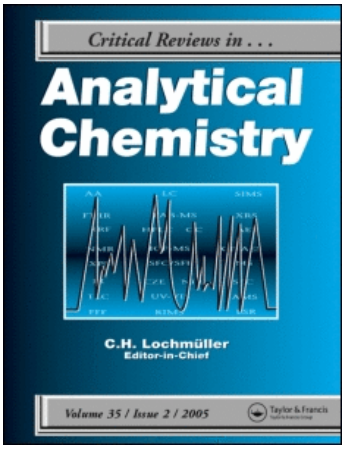

Critical Reviews in Analytical Chemistry
Publication details, including instructions for authors and subscription information:
http://www.informaworld.com/smpp/title~content=t713400837

ELECTROCHEMISTRY IN THIN LAYERS OF SOLUTION

A. T. Hubbard; D. G. Peters

To cite this Article Hubbard, A. T. and Peters, D. G.(1973) 'ELECTROCHEMISTRY IN THIN LAYERS OF SOLUTION', Critical Reviews in Analytical Chemistry, 3: 2, 201 — 242
To link to this Article: DOI: 10.1080/10408347308542661
URL: http://dx.doi.org/10.1080/10408347308542661

ELECTROCHEMISTRY IN THIN LAYERS OF SOLUTION

Author: **A. T. Hubbard**
Department of Chemistry
University of Hawaii
Honolulu, Hawaii

Referee: **D. G. Peters**
Department of Chemistry
Indiana University
Bloomington, Ind.

TABLE OF CONTENTS

I. INTRODUCTION

Thin-layer electrodes (TLE) confine the reactant within a 10^{-3}-cm layer at the electrode surface. As a result, each reactant particle has immediate access to the electrode surface. Mass-transfer equilibrium is achieved sufficiently rapidly so that the complicated transport behavior associated with conventional electrodes can generally be avoided. Accordingly, the equations governing thin-layer electrodes are simple combinations of Faraday's law and the Nernst equation or the equation describing the rate of electron transfer at an electrode. Surface-active impurities are virtually excluded from the electrode surface unless they are present at high concentrations.

Thin-layer electrodes employ lower direct-current densities than for conventional electrodes, making them well suited for the study of slow electrode reactions. On the other hand, the a.c. impedances of thin-layer electrodes can be analyzed to evaluate the rates of fast reactions.

Because thin-layer electrodes provide clean surfaces and obey very simple experimental equations, they are very useful in attempts to combine electrochemical techniques with electron and photon spectroscopy in order to study the relationship between electrochemical behavior and such aspects of the surface state as its atomic and electronic structure and elemental composition.

The theory and practice of electrochemistry with thin-layer cells were reviewed recently.[1] Developments too recent for that review are presented here along with the essential experimental equations, instrumentation, and applications.

II. EXPERIMENTAL EQUATIONS

A. Voltammetry[2,3]

Linear-potential-sweep voltammetry is generally a convenient starting point for TLE studies of new systems, often providing an indication as to the concentration, reaction rates, formal or standard potentials, stoichiometries, electrical double layer dependences, and n values of the reactant couples, including those stemming from the electrode material and solvent. Most reactions proceed to completion within about ± 2RT/F V of their peak potentials and the products are retained in the thin-layer cavity for examination on subsequent scans. Thus, a rather complete description of even a complicated reaction sequence can often be obtained from a single repetitive-scan experiment.

1. Reversible Reactions (Soluble Components)

If the electrode reaction (Equation 1)

$$Ox + ne^- \rightleftharpoons R \qquad (1)$$

obeys the Nernst equation during the potential scan, if all species are soluble, and if the rate of

potential scan is sufficiently low (see below), then the current-potential curve follows Equation 2

$$i = \frac{n^2F^2VC^0(-r)}{RT} \left\{ \frac{\exp\left[\frac{nF}{RT}(E - E^0)\right]}{1 + \exp\left[\frac{nF}{RT}(E - E^0)\right]} \right\}^2 \qquad (2)$$

where the symbols are as defined in Part F of this Section. A graph of Equation 2 appears in Figure 1. The peak current, i_p, which occurs at the formal standard potential, $E = E^0$, is given by Equation 3

$$i_p = \frac{n^2F^2(-r)VC^0}{4RT} \qquad (3)$$

Equality of the peak potentials for cathodic and anodic scans has proved to be a sensitive criterion of electrochemical reversibility. Since the reduction or oxidation of the reactant proceeds to completion during the anodic or cathodic scan, the total charge corresponding to the time integral of the current-potential curve is given by Faraday's law:

$$Q = nFVC^0 \qquad (4)$$

Comparison of Equations 3 and 4 indicates that n and C^0 may be determined independently from the current-potential curve and its time integral, because i_p varies as the square of n, whereas Q varies linearly with n.

A simple subtraction of the current observed in the absence of reactant usually suffices to correct the current observed with the reactant solution for background contributions due to the solvent and electrode surface. Exceptions to this rule occur with chemisorbed reactants, as described in Part IV, Section C.

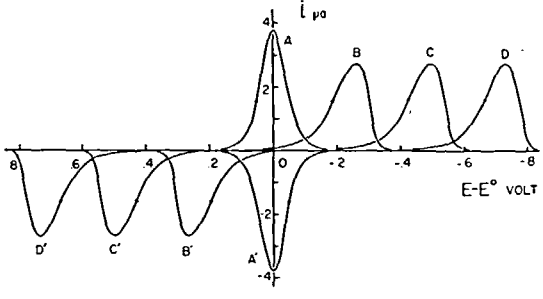

FIGURE 1. Theoretical thin-layer cyclic current-potential curves for soluble reactants. Graphs of Equations 2, 19, and 20. Curve A. Reversible reaction ($*k^0 \geq 10^{-3}$ cm sec^{-1}); Curve B. $*k^0 = 10^{-6}$ cm sec^{-1}; Curve C. $*k^0 = 10^{-8}$ cm sec^{-1}; and Curve D. $*k^0 = 10^{-10}$ cm sec^{-1}. The following values of the parameters were assumed in making the graphs: A = 0.5 cm^2; $*\alpha = 0.5$; $C^0 = 10^{-6}$ mol cm^{-3}; F = 9.65 x 10^4 coul equiv^{-1}; n = 1; v = 2 mV sec^{-1}; T = 298°K; and V = 2 x 10^{-3} cm^3. (Reprinted from Reference 2 by courtesy of Elsevier Publishing Co.)

2. Limitations on Sweep Rate for Thin-layer Voltammetry

The conditions under which the observed current is not limited appreciably by diffusion and Equation 1 is accurately obeyed can be determined by solving Fick's second law (Equation 5)

$$\frac{\partial C_{Ox}(x,t)}{\partial t} = D_{Ox} \frac{\partial^2 C_{Ox}(x,t)}{\partial x^2} \qquad (5)$$

subject to the initial condition that the initial concentration is uniform throughout the thin-layer cavity (apart from the double-layer region), and to the boundary condition that the surface concentration is given by the Nernst equation

$$E = E^0 + \frac{RT}{nF} \ln \frac{C_{Ox}}{C_R} \qquad (6)$$

The analogous problem in heat diffusion is discussed by Carslaw and Jaeger;[4] the solution is

$$C_{Ox} = C^0_{Ox} \sum_{m=0}^{\infty} \exp\left[\frac{-(2m+1)^2 \pi^2 D_{Ox} t}{\ell^2}\right] \sin \frac{(2m+1)\pi x}{\ell} \times \left\{ \frac{4}{(2m+1)\pi} + (2m+1) \frac{4D_{Ox}\pi}{\ell^2} \times \int_0^t \frac{\exp[(2m+1)^2 \pi^2 D_{Ox} y/\ell^2]}{1 + \exp\{nF/RT)[E - E(0)] - ry\}} dy \right\} \qquad (7)$$

If the sweep rate r is sufficiently low, the y-dependent term, ry, in the denominator of the integrand of Equation 7 can be neglected. Integration of this approximate form of Equation 7 then yields the Nernst equation

$$E = E^0 + \frac{RT}{nF} \ln \frac{C_{Ox}}{C^0 - C_{Ox}} \qquad (8)$$

in a form which is applicable to thin-layer electrodes so long as the concentrations are uniform within the solution layer:

$$C^0 = C_{Ox} + C_R \qquad (9)$$

These circumstances exist[3,5] whenever r meets the conditions specified by Equation 10

$$|r| \leq \frac{RT}{nF}\frac{\pi^2 D}{3l^2}\log\frac{1+\epsilon}{1-\epsilon} \qquad (10)$$

where ϵ is the maximum relative error in applying Equation 2. For example, if $l = 10^{-3}$ cm, $D = 10^{-5}$ cm^2 sec^{-1}, and T = 300°K, then i is given by Equation 2 within a relative error ϵ whenever the magnitude of r is less than 10 mV sec^{-1}.

Although each new experimental case could be treated by solving the diffusion equation and simplifying the result appropriately to thin-layer conditions, it is expedient to assume from the outset that thin-layer conditions (e.g., Equation 10) have been achieved. For instance, Equation 2 can be obtained by differentiating Faraday's law, Equation 4, with respect to t and combining the result

$$i = nFV\frac{dC_{Ox}}{dt} \qquad (11)$$

with the Nernst equation, Equation 8.

3. Reversible Reactions (One Component Insoluble)

Reversible deposition of a metal on an electrode of the same metal

$$M^{n+} + ne^- \rightleftharpoons M \qquad (12)$$

follows Equation 13 of which a graph appears in Figure 2

$$i = \frac{n^2F^2V(-r)}{RT}\exp\left[\frac{nF}{RT}(E - E^0)\right] \qquad (13)$$

The variation of the current with potential is purely exponential and changes between the positive and negative segments of the curve instantaneously upon reversal of the direction of potential scan. Rather different equations are required to describe the deposition of a metallic monolayer on an electrode of some other metal, as described in Section D of Part IV.

4. Totally Irreversible Reactions

In the event that the electrode reaction is sufficiently slow that it does not obey the Nernst equation while the thin-layer current-potential curve is being recorded, the above equations do not apply. Instead, the current-potential expression is obtained by combining Faraday's law, in differential form, Equation 11, with the electrode rate expression appropriate to the reaction of interest. For instance, suppose that the reaction ($Ox + ne^- \rightleftharpoons R$) follows the rate law

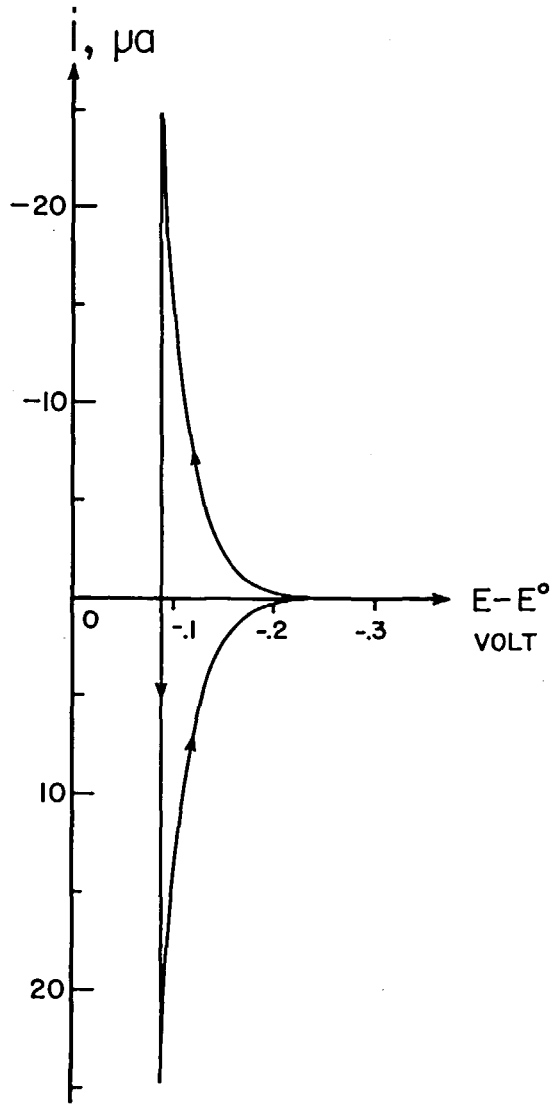

FIGURE 2. Theoretical thin-layer cyclic current-potential curve for reversible deposition and dissolution of a metal. Graph of Equation 13 for n = 1, V = 10^{-3} cm^3, |r| = 2 mV sec^{-1}, and T = 298°K.

$$i = nFA\,{}^*k^0\left\{C_{Ox}\exp\left[\frac{-{}^*\alpha F}{RT}(E - E^0)\right] - C_R\exp\left[\frac{(1 - {}^*\alpha)F}{RT}(E - E^0)\right]\right\} \qquad (14)$$

If $^*k^0$ is greater than 10^{-4} cm sec^{-1}, then the reversible theory applies (cases i and ii, above). However, for $^*k^0 \leq 10^{-5}$ cm sec^{-1}, equations appropriate to irreversible behavior must be derived. The contribution of the backward reaction to the net current will be negligible (see Part II, Section A-5) so that Equation 14 becomes identical with Equation 15

$$ {}_{c}i = nFA\ {}^{*}k^{0}\ C_{Ox} \exp\left[\frac{-{}^{*}\alpha F}{RT}(E - E^{0})\right] \qquad (15) $$

for reductions, or with Equation 16 for oxidations

$$ {}_{a}i = -nFA\ {}^{*}k^{0}\ C_{R} \exp\left[\frac{(1 - {}^{*}\alpha)F}{RT}(E - E^{0})\right] \qquad (16) $$

Combining Equation 15 or Equation 16 with Equation 11 and integrating with respect to t gives

$$ C_{Ox} = C^{0} \exp\left\{\frac{ART\ {}^{*}k^{0}}{-{}^{*}\alpha rFV} \exp\left[\frac{-{}^{*}\alpha F}{RT}(E - E^{0})\right]\right\} \qquad (17) $$

$$ C_{R} = C^{0} \exp\left\{\frac{-ART\ {}^{*}k^{0}}{(1 - {}^{*}\alpha)rFV} \exp\left[\frac{(1 - {}^{*}\alpha)F}{RT}(E - E^{0})\right]\right\} \qquad (18) $$

Inserting these expressions for C_{Ox} and C_{R} into the rate equations yields the current-potential expressions for totally irreversible reduction or oxidation reactions, respectively

$$ {}_{c}i = nFA\ {}^{*}k^{0}\ C^{0} \exp\left\{\frac{-{}^{*}\alpha F}{RT}(E - E^{0}) + \frac{ART\ {}^{*}k^{0}}{{}^{*}\alpha FVr} \exp\left[\frac{-{}^{*}\alpha F}{RT}(E - E^{0})\right]\right\} \qquad (19) $$

$$ {}_{a}i = nFA\ {}^{*}k^{0}\ C^{0} \exp\left\{\frac{(1 - {}^{*}\alpha)F}{RT}(E - E^{0}) - \frac{ART\ {}^{*}k^{0}}{(1 - {}^{*}\alpha)FVr} \exp\left[\frac{(1 - {}^{*}\alpha)F}{RT}(E - E^{0})\right]\right\} \qquad (20) $$

Graphs of Equations 19 and 20 for various assumed values of $*k^{0}$ appear in Figure 1. The separation in potential between the anodic and cathodic peaks is seen to increase as $*k^{0}$ decreases, but the shape of the curves is independent of $*k^{0}$ for totally irreversible reactions. The breadth of the curves increases as $*\alpha$ decreases, as illustrated in Figure 3.

The cathodic and anodic peak currents are given by Equations 21 and 22

$$ {}_{c}i_{p} = \frac{{}^{*}\alpha nF^{2}V(-r)C^{0}}{eRT} \qquad (21) $$

$$ {}_{a}i_{p} = \frac{-(1 - {}^{*}\alpha)nF^{2}VrC^{0}}{eRT} \qquad (22) $$

from which it can be seen that the parameters $*\alpha$ and $(1-*\alpha)$ are proportional to the measured peak currents. The peak potentials are given by Equations 23 and 24.

$$ {}_{c}E_{p} = E^{0} + \frac{RT}{{}^{*}\alpha F} \ln\left[\frac{ART\ {}^{*}k^{0}}{{}^{*}\alpha F(-r)V}\right] \qquad (23) $$

$$ {}_{a}E_{p} = E^{0} - \frac{RT}{(1 - {}^{*}\alpha)F} \ln\left[\frac{ART\ {}^{*}k^{0}}{(1 - {}^{*}\alpha)FrV}\right] \qquad (24) $$

Substituting Equations 21 and 22, which describe $*\alpha$ and $(1-*\alpha)$ in terms of the peak current, into

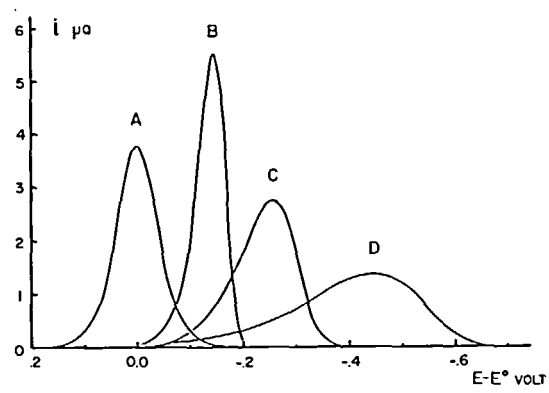

FIGURE 3. Theoretical thin-layer current-potential curves. Curve A. Reversible reaction ($*k^{0} > 10^{-4}$ cm sec^{-1}); Curve B. $*\alpha = 0.75$; Curve C. $*\alpha = 0.50$; and Curve D. $*\alpha = 0.25$. The values employed in making the graphs were A = 0.5 cm^{2}; $C^{0} = 10^{-6}$ mol cm^{-3}; $*k^{0} = 10^{-6}$ cm sec^{-1}; n = 1; $|r| = 2$ mV sec^{-1}; and V = 10^{-3} cm^{3}. (Reprinted from Reference 2 by courtesy of Elsevier Publishing Co.)

Equations 23 and 24 gives $*k^{0}$ explicitly:

$$ {}^{*}k^{0} = \frac{{}_{c}i_{p}\ e}{nFAC^{0}} \exp\left[\frac{e\ {}_{c}i_{p}({}_{c}E_{p} - E^{0})}{nFV(-r)C^{0}}\right] \qquad (25) $$

$$ {}^{*}k^{0} = \frac{{}_{a}i_{p}\ e}{nFAC^{0}} \exp\left[\frac{e\ {}_{a}i_{p}({}_{a}E_{p} - E^{0})}{nFVrC^{0}}\right] \qquad (26) $$

That is, $*k^{0}$ can be determined directly from the current and potential at the peak. It varies logarithmically with $({}_{c}E_{p}-E^{0})$ or $({}_{a}E_{p}-E^{0})$, starting from about 10^{-5} cm sec^{-1} and decreasing by a factor of ten for each 120-mV increase. In the event that the standard potential is not known with certainty, the value of $*k^{0}$ can be estimated simply from the potentials of the cathodic and anodic peaks. Eliminating E° between Equations 25 and 26 and solving for $*k^{0}$ gives

$$ {}^{*}k^{0} = \left\{\frac{{}_{c}i_{p}\ e}{nFAC^{0}}\left[\frac{-{}_{a}i_{p}\ e}{nFAC^{0}}\right]^{-{}_{c}i_{p}/{}_{a}i_{p}} \times \exp\left[\frac{-{}_{c}i_{p}\ e}{nFV\ r\ C^{0}}({}_{a}E_{p} - {}_{c}E_{p})\right]\right\}^{{}_{a}i_{p}/({}_{a}i_{p}-{}_{c}i_{p})} \qquad (27) $$

Combining Equations 21 and 22 leads to the analogous expression for $*\alpha$:

$$ {}^{*}\alpha = \frac{{}_{c}i_{p}}{{}_{c}i_{p} - {}_{a}i_{p}} \qquad (28) $$

5. Conditions for Total Irreversibility in Thin-layer Voltammetry

The totally irreversible electrode behavior described by the above equations is observed when $*k^0$ is within the limits indicated by Equations 29 and 30:

$$*k^0 \leq \frac{*\alpha F|r|V}{ART}\,\epsilon^{*\alpha} \qquad \text{(reduction)} \qquad (29)$$

$$*k^0 \leq \frac{(1-*\alpha)F|r|V}{ART}\,\epsilon^{(1-*\alpha)} \qquad \text{(oxidation)} \qquad (30)$$

where ϵ is the relative error in the predicted net current due to neglect of the backward current component. For example, if A = 1 cm^2, $\alpha = 0.5$, r = 2 mV sec^{-1}, T = 300°K, V = 10^{-3} cm^3, then the current will be given by Equations 19 and 20 within a relative error, ϵ, less than 0.01, so long as $*k^0 \leqslant 4 \times 10^{-6}$ cm sec^{-1}. Equations 29 and 30 are mathematical consequences of requiring ${}_ai/{}_ci \leqslant \epsilon$ for a negative-going potential scan, or ${}_ci/{}_ai \leqslant \epsilon$ for a positive scan. Thus, expressing ${}_ai/{}_ci$ in terms of Equations 15 and 16 gives

$${}_ai/{}_ci = \exp\left[\frac{F}{RT}(E - E^0)\right]\frac{C_R}{C^0 - C_R} \qquad (31)$$

A simple but adequate representation of C_R is provided by the inequalities

$$C_R \leq \int_0^t {}_ci\,dt/nFV \leq \int_0^\tau \frac{A\,*k^0\,C^0}{V} \times \exp\left[\frac{-*\alpha F}{RT}(E - E^0)\right]dt \qquad (32)$$

so that Equation 31 becomes

$$\exp\left[\frac{F}{RT}(E - E^0)\right] \times \left\{\frac{1}{1 - \frac{A\,*k^0}{V}\int_0^\tau \exp\left[\frac{-*\alpha F}{RT}(E - E^0)\right]dt} - 1\right\} \leq \epsilon \qquad (33)$$

where $\tau \equiv [{}_cE_p - E(0)]/r = \{E^0 - E(0) + \frac{RT}{*\alpha F}\ln[\frac{ART*k^0}{*\alpha F(-r)V}]\}$ and $E \equiv E(0) + rt$. Integration and collection of terms gives Equation 29. Equation 30 is derived similarly.

6. Influence of the Diffuse Layer on the Magnitude of *α and $*k^0$

The values of *α and $*k^0$ depend in part on the energies and symmetries of the electronic levels of the electrode, reactant, and electrolyte, particularly the occupied levels of highest energy and unoccupied levels of lowest energy that have symmetries appropriate for interaction in the transition state.[6] However, *α and $*k^0$ also vary nonspecifically with the electric field in the interface and the ionic charge of the reactant, as described below. Studies of specific molecular electronic influence on electrode reactions by means of thin-layer electrodes are presented in Part IV, Sections B and C.

If the average electrical potential of the reaction plane relative to the bulk of the solution is Φ_2, then the concentration at the reaction plane will be given by

$${}_iC_2 = {}_iC_b \exp\left[\frac{-Z_iF}{RT}\right]_i\Phi_2 \qquad (34)$$

where Z_i is the ionic charge of the i^{th} species.[7] Furthermore, the potential Φ_2 must be subtracted from the total difference of potential across the interface. Accordingly, Equation 15 for the rate of reduction becomes

$${}_ci = nFA\,*k^0\,C_{Ox}\exp\left[\frac{-*\alpha F}{RT}(E - E^0 - {}_{Ox}\Phi_2) \times \frac{-Z_{Ox}F}{RT}\,{}_{Ox}\Phi_2\right] \qquad (35)$$

Similarly, for oxidations:

$${}_ai = nFA\,*k^0\,C_R\exp\left[\frac{(1-*\alpha)F}{RT}(E - E^0 - {}_R\Phi_2) - \frac{Z_RF}{RT}\,{}_R\Phi_2\right] \qquad (36)$$

Since Φ_2 is generally not known independently as a function of E, Equations 35 and 36 cannot be employed directly in treating the current-potential data. Instead, an effective approximate approach has been developed:[8-10] It represents the interface, over the narrow interval of the current-potential curve (about 200 mV), as a "double layer" consisting of compact and diffuse regions which behave as do capacitors connected in series. Combining the definition of capacitance with the equation for the equivalent capacitance of a series combination yields

$$Q = C_d\Phi_2 = C(E - E_z) = \left(\frac{1}{C_d} + \frac{1}{C_c}\right)^{-1}(E - E_z) \qquad (37)$$

Solving for Φ_2 gives

$$\Phi_2 = \frac{C}{C_d}(E - E_z) \qquad (38)$$

Introducing the description of Φ_2 provided by Equation 38 into Equations 35 and 36 and combining terms leads to expressions which are identical with Equations 15 and 16:

$$_{c}i = nFA\ {}^{*}k^{0}\ C_{Ox}\ \exp\left[\frac{-{}^{*}\alpha F}{RT}(E - E^{0})\right] \quad (15)$$

$$_{a}i = nFA\ {}^{*}k^{0}\ C_{R}\ \exp\left[\frac{(1 - {}^{*}\alpha)F}{RT}(E - E^{0})\right] \quad (16)$$

except that the apparent quantities $*k^0$ and $*\alpha$ are now defined in terms of the diffuse-layer-independent quantities k^0 and α according to Equations 39 through 42:

$$*k^{0} = k^{0}\ \exp\left[(\alpha - Z_{Ox})\frac{F}{RT}\ {}_{Ox}\Phi_{2}\right] \quad (39)$$

$$*k^{0} = k^{0}\ \exp\left[(1 - \alpha - Z_{R})\frac{F}{RT}\ {}_{R}\Phi_{2}\right] \quad (40)$$

$$*\alpha = \alpha - \frac{C}{C_{d}}(\alpha - Z_{Ox}) \quad (41)$$

$$(1 - *\alpha) = 1 - \alpha - \frac{C}{C_{d}}(1 - \alpha + Z_{R}) \quad (42)$$

That is, the form of the rate law is not altered by making allowance for the influence of the diffuse double layer potential. The diffuse-layer-dependent "apparent" rate parameters, $*k^0$ and $*\alpha$, are thus related to the fundamental quantities, k^0 and α, by means of simple equations. Values of C may be obtained from tables of differential capacitance data, and C_d is commonly estimated with the use of the Gouy-Chapman-Stern model of the interface.[7] Values of C/C_d between 0.05 and 0.07 are typical for 1 *N* electrolytes. As ϕ_2 increases, the peak shifts toward less reversible potentials unless $Z\ \Phi_2$ is negative, and the peak current decreases except when a cation is being reduced or an anion oxidized.

It may be worth pointing out that Equations 37 to 42, which describe the influences of the diffuse layer on $*\alpha$ and $*k^0$, do not depend on the measuring technique employed and are therefore applicable also to each of the studies described below.

B. Coulometry

As was mentioned in connection with Equation 4, the area under the thin-layer current-potential curve is given by Faraday's law and corresponds to the charge required to electrolyze all of the reactant in the thin layer. In order to minimize contributions to the final reading from background reactions and drift in the electronic circuitry, it is advantageous to switch the potentiostat setting instantly from a potential in front of the peak to a value past the peak at which the reaction goes virtually to completion, electronically integrating the resulting current. If the starting reactant is not absorbed to an appreciable extent, then the limiting charge, Q, is given by

$$|Q - Q_{b}| = nFVC^{0} \quad (43)$$

where Q_b, the value of the charge in the absence of the reactant, includes contributions from double-layer charging (about 10 μc cm^{-2}) and from electrolysis of the solvent, electrolyte, and electrode surface (about 30 to 100 μc cm^{-2}). Typically, it is the accuracy with which Q_b can be determined that controls the accuracy of the analysis. For analytical purposes, the initial concentration of the reactant should be made reasonably large (5×10^{-3} to 0.1 *N*), so that charge consumed by the reactant ($nFVC^0$) will be relatively large (about 10^3 to 2×10^4 μc per cm^2 of electrode cross-sectional area) in comparison with Q_b.

If the reactant is adsorbed onto the electrode surface and if the adsorbed species is electrochemically reactive, Equation 44 does not apply; instead:[11]

$$|Q - Q_{b}| = nFVC^{0} + nF\Gamma \quad (45)$$

Systems in which Q_b could not be assumed to be independent of Γ have been encountered, and have been treated as described in Part IV, Section C. The limit of sensitivity of thin-layer coulometry for detection of adsorbed reactants is established by the thickness of the solution layer, $\ell = V/A$, and the accuracy with which $(Q-Q_b)$ can be determined. For example, if n = 1, $V = 2 \times 10^{-3}$ cm^3, $C^0 = 10^{-3}$ *F* and A = 1 cm^2, then the amount of charge consumed by electrolysis of dissolved reactant (about 200 μc) will be comparable to that for a monolayer (about 2×10^{-9} mol cm^{-2}) of adsorbed reactant (about 200 μc). Thus, if $(Q-Q_b)$ can be determined with ± 1% for a 1 mF solution of the reactant, the limit of detectability is about 0.01 monolayer (2×10^{-11} mol cm^{-2}). In addition to being rather sensitive to the occurrence of adsorption, the thin-layer-electrode approach avoids the physical uncertainty and mathematical complexity of conventional methods. Instances of the use of thin-layer coulometry for the determination of adsorbed reactants are enumerated in Part IV, Section C.

When the current that flows during a thin-layer coulometric measurement is diffusion-controlled,

the final value of Q is reached within about 0.1 sec. However, a longer time is commonly required due to the influence of ohmic polarization and electron-transfer-controlled background reactions. Ohmic polarization does not seriously affect normal thin-layer coulometric measurements in the presence of strong electrolytes; however, rapid completion of the electrolysis, even in weak electrolytes, can be accomplished by means of porous-boundary[1,2] thin-layer electrodes (see Part III, Section A). Background reactions occurring at solid electrodes tend to produce currents that do not decrease rapidly to zero, giving rise to charge-time plots of nonzero final slope; it is generally observed, however, that the reactant and blank curves become identical in slope once complete electrolysis of the reactant has taken place, and correct results are obtained when Q and Q_b are evaluated anywhere in the region where these slopes are identical.

The experimental factors that dictate the time scale for thin-layer coulometry of diffusion-controlled systems have been identified by calculating $Q(t)-Q_b(t)$, taking diffusion into account.[3] In particular, if the reaction (Equation 1) obeys the Nernst equation, and if at $t = 0$ the potential is adjusted instantly to a value at which the reaction begins to take place at a diffusion-controlled rate, then the concentration of Ox will be[4]

$$C_{Ox}(x,t) = \frac{4}{\pi} C^0 \sum_{m=1}^{\infty} \frac{1}{2m-1} \times \exp\left[\frac{-(2m-1)^2 \pi^2 D_{Ox} t}{\ell^2}\right] \sin\frac{(2m-1)\pi x}{\ell} \quad (46)$$

The current and charge follow from Equation 46:

$$i - i_b = nFAD_{Ox}\left(\frac{dC_{Ox(x,t)}}{dx}\right)_{x=0} = \frac{4nFAD_{Ox}C^0}{\ell} \sum_{m=1}^{\infty} \exp\left[\frac{-(2m-1)^2 \pi^2 D_{Ox} t}{\ell^2}\right] \quad (47)$$

$$Q(t) - Q_b(t) = nFAVC_{Ox} \times \left\{1 - \frac{8}{\pi^2} \sum_{m=1}^{\infty} \left(\frac{1}{2m-1}\right)^2 \exp\left[\frac{-(2m-1)^2 \pi^2 D_{Ox} t}{\ell^2}\right]\right\} \quad (48)$$

The difference $Q(t)-Q_b(t)$ approaches its limiting value, $nFVC^0$, within a relative error less than ϵ, defined by Equation 49, for durations given by Equation 50.

$$\epsilon \equiv \frac{nFVC^0 - [Q(t) - Q_b(t)]}{nFVC^0} \quad (49)$$

$$t = \frac{\ell^2 |\ln \epsilon|}{\pi^2 D_{Ox}} \quad (50)$$

Equation 50 was obtained from Equation 48 by noting that terms for which $m > 1$ are negligibly small, combining the result with the definition of ϵ, Equation 49, and solving for t. For example, if $D_{Ox} = 10^{-5}$ cm^2 sec^{-1}, $\epsilon = 0.001$, and $\ell = 10^{-3}$ cm, then the duration t must be 0.07 sec in order for a relative error of less than 0.1% to be expected.

If the rate of the electron-transfer step is so slow that the current is not diffusion-controlled, the time required for completion of the electrolysis will be larger than that predicted by Equation 50. Combining Equations 11 and 15 gives

$$\frac{dC_{Ox}}{dt} = \frac{A\, {}^*k^0\, C_{Ox}}{V} \exp\left[\frac{-{}^*\alpha F}{RT}(E - E^0)\right] \quad (51)$$

which after integration yields

$$C_{Ox} = C^0 \exp\left\{\frac{-A\, {}^*k^0\, t}{V} \exp\left[\frac{-{}^*\alpha F}{RT}(E - E^0)\right]\right\} \quad (52)$$

$$i - i_b = nFA\, {}^*k^0\, C^0 \times\left\{\exp\left[\frac{-{}^*\alpha F}{RT}(E - E^0)\right] - \frac{A}{V} {}^*k^0\, t \exp\left[\frac{-{}^*\alpha F}{RT}(E-E^0)\right]\right\} \quad (53)$$

A second integration leads to Equation 54

$$|Q - Q_b| = nFVC^0 \left\{1 - \exp\left[\frac{-A\, {}^*k^0\, t}{V} \exp\frac{-{}^*\alpha F}{RT}(E-E^0)\right]\right\} \quad (54)$$

which when combined with Equation 49 gives the desired expression:

$$t = \frac{V}{A\, {}^*k^0} \exp\left[\frac{{}^*\alpha F}{RT}(E - E^0)\right] \ln\frac{1}{\epsilon} \quad (55)$$

For instance, if $A = 0.5$ cm^2, $\epsilon = 10^{-2}$, ${}^*k^0 \exp[-{}^*\alpha F(E-E^0)/RT] = 10^{-5}$ cm sec^{-1}, and $V = 10^{-3}$ cm^3, then $t = 92$ sec. Several hours would be required for completion of this electrolysis using cells of conventional designs.

C. Chronopotentiometry[3,13]

The realization that under certain experimental conditions thin-layer electrodes offer useful simplifications apparently stems from a paper by

Christensen and Anson,[13] in which the theory and practice of thin-layer chronopotentiometry are described. The simplicity in circuitry and experimental equations associated with the use of constant current make chronopotentiometry the approach of choice for certain applications, although it has been supplanted by approaches based upon control of the potential owing to difficulties in determining the chronopotentiometric transition time, τ, from the experimental curves, and in correcting τ for the contribution due to background reactions. Of particular usefulness is the fact that the "descriptive" parameters such as E^0, $^*\alpha$ and $^*k^0$ as well as the "quantitative" characteristics such as C^0 and n can be determined directly from the experimental curves for well-behaved systems.

1. Reversible Reactions (Soluble Components)

The chronopotentiometric potential-time equation for reversible reduction of Ox according to the reaction depicted in Equation 1 follows immediately from the Nernst equation (Equation 6), in which C_R has been calculated from Faraday's law, written in the form of Equation 56

$$C_R = it/nFV \tag{56}$$

when the current density is so small that the thin layer of solution remains homogeneous (Equation 9); the result is

$$E = E^0 + \frac{RT}{nF} \ell n \left[\frac{nFVC^0}{it} - 1 \right] \tag{57}$$

A graph of Equation 58 appears in Figure 4. The anodic potential-time curve follows a similar equation:

$$E = E^0 - \frac{RT}{nF} \ell n \left[\frac{nFVC^0}{it} - 1 \right] \tag{58}$$

The potential, $E_{1/2}$, corresponding to $t = \tau/2$, is equal to the formal potential. The transition time, τ, corresponding to complete electrolysis of the reactant is given by Equation 59.

$$\tau = nFVC^0/i \tag{59}$$

Equations 57 to 59 apply without change to cyclic chronopotentiograms for any number of cycles. In the event that the charge consumed by background reactions cannot be neglected, Equation 59 does not apply; instead:

$$i\tau = nFVC^0 + Q_b \tag{60}$$

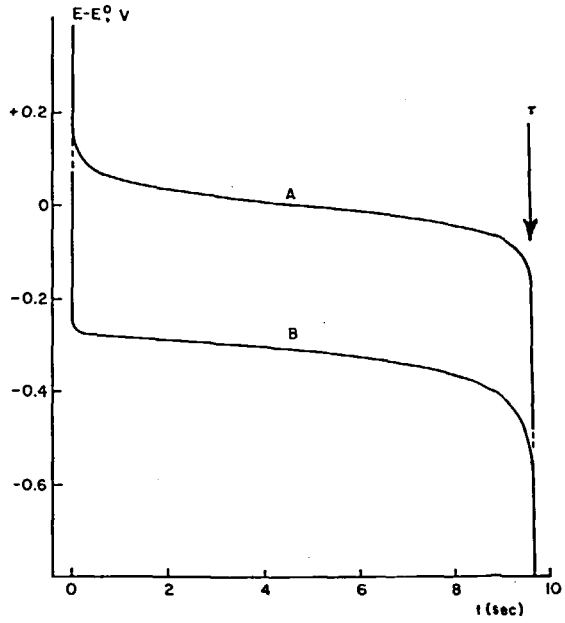

FIGURE 4. Theoretical thin-layer chronopotentiometric potential-time curves.[3] Curve A. Reversible reduction ($^*k^0 \geq 10^{-3}$ cm sec^{-1}) and Curve B. Irreversible reduction ($^*k^0 = 10^{-6}$ cm sec^{-1}). Values of the parameters assumed in making the plots were A = 0.5 cm^2, $^*\alpha$ = 0.5 cm^2, $C^0 = 10^{-3}$ *F*, i = 10 μa, n = 1, T = 298°K, and V = 10^{-3} cm^3.

The correct procedure for determining Q_b from an experimental curve depends in a detailed way on the current-potential characteristics of the background reaction. For instance, if the background charge is due primarily to reversible processes, such as the charging of the diffuse region of the double layer or the reversible electrolysis of a competing reactant, then it can be obtained from measurement of the charge required, in the absence of the reactant, to reach some particular potential associated with the transition time for the reactant

$$Q_b = i\tau_b \tag{61}$$

However, if the background reaction proceeds irreversibly, correction for background charge requires the evaluation, by some means, of the integral term in Equation 62:

$$Q_b = \int_0^\tau i_b[E(t)]\, dt \tag{62}$$

where i_b [E(t)] is a description of the background current as a function of time; difficulty arises from the fact that this function depends on the manner

in which the potential varies with time in the presence of the reactant. The background reaction also has the effect of decreasing the slope of the chronopotentiogram at the completion of the electrolysis, making location of the transition time more difficult.

2. Irreversible Reactions (Soluble Components)

If the rate of the reaction ($Ox + ne^- \rightleftharpoons R$) obeys Equation 15 or Equation 16, and if the current density is sufficiently small for Equation 9 to apply, then the thin-layer chronopotentiometric potential-time curve is described by Equation 63 (for reduction) or Equation 64 (for oxidation):

$$E - E^0 = \frac{RT}{{}^*\alpha F} \ln\left[\frac{nFA\ {}^*k^0}{i}\left(c^0 - \frac{it}{nFV}\right)\right] \quad (63)$$

$$E - E^0 = \frac{-RT}{(1 - {}^*\alpha)F} \ln\left[\frac{-nFA\ {}^*k^0}{i}\left(c^0 + \frac{it}{nFV}\right)\right] \quad (64)$$

In these equations anodic currents are, as usual, taken to be negative. Equation 63 is graphed in Figure 4. As before, the value of τ is given by Equation 59. Hence, if $E\text{-}E^0$ is plotted against $\ln [C^0\text{-}|i|t/(nFV)]$, a straight line is obtained; its slope is equal to $RT/({}^*\alpha F)$ or $-RT/[(1-{}^*\alpha)F]$ and its intercept is equal to $[\ln(nFA\ {}^*k^0/i)]\,RT/({}^*\alpha F)$ or $[\ln(nFA\ {}^*k^0/i)RT/[(1-{}^*\alpha)F]$ for reduction or oxidation, respectively.

3. Limitations on the Current Density for Thin-layer Chronopotentiometry

An expression for the concentration of Ox, C_{Ox} (x, t) in the thin-layer cell under conditions of constant current density with control of the potential by diffusion can be obtained by solving Fick's second law, Equation 5, subject to a boundary condition (Equation 65) that corresponds to constancy of the flux at the electrode surface:

$$i = nFAD_{Ox}\left(\frac{\partial C_{Ox}}{\partial x}\right)_{x=0} \quad (65)$$

The result is[4]

$$C_{Ox} = c^0 - \frac{it}{nFV} - \frac{i\ell}{nFAD_{Ox}}\left\{\frac{2\ell^2 - 6x + 3x^2}{6\ell^2} - \frac{2}{\pi^2}\sum_{m=1}^{\infty}\frac{(-1)^m}{m^2}\exp\left[\frac{-m^2\pi^2 D_{Ox}t}{\ell^2}\right]\cos\left[\frac{m\pi(\ell-x)}{\ell}\right]\right\} \quad (66)$$

The transition time calculated from Equation 59, which assumes thin-layer conditions, will be correct within a relative error ϵ so long as the total quantity of reactant remaining in the thin-layer cavity is less than $\epsilon C^0 V$. That is, it is sufficient to require that the average concentration, $\overline{C_{Ox}}$, at $t = \tau$ be given by

$$\overline{C_{Ox}}(\tau) \equiv c^0 - \frac{i\tau}{nFV} \leq \epsilon c^0 \quad (67)$$

The exponential terms in Equation 66 are vanishingly small under the experimental conditions normally employed, so that

$$c^0 - \frac{i\tau}{nFV} = \frac{i\ell}{3nFAD_{Ox}} \approx \frac{\ell^2 c^0}{3D_{Ox}} \leq \epsilon c^0 \quad (68)$$

Thus, thin-layer conditions are expected to hold whenever

$$\tau \geq \frac{\ell^2}{3D_{Ox}} \quad (69)$$

For example, if $D_{Ox} = 10^{-5}$ cm sec^{-1}, $\epsilon = 0.01$, and $\ell = 10^{-3}$ cm, then i and C^0 should be arranged so that $\tau \geq 3.3$ sec.

D. A.C. Voltammetry

When a small, rapidly alternating voltage is superimposed on the nominal potential of a thin-layer electrode, the direct-current behavior of the electrode is unaffected. For example, when a sinusoidal signal of amplitude, V_p, about 5mV and angular frequency, ω, above about 150 rad sec^{-1} is combined with a potential scan (Equation 70),

$$E = E(0) + rt + V_p \sin \omega t \quad (70)$$

the d.c. signal obeys the usual equations for thin-layer linear-potential-scan voltammetry (Part II, Section A). The a.c. component, I, follows Equation 71

$$I = \frac{V_p \sin \omega t}{Z} \quad (71)$$

in which Z is the effective electrode impedance. Thus, the impedance of cell can be evaluated from measurements of the amplitude, $|I|$, and phase angle, Φ_I, of the a.c. component:

$$Z = \left(\frac{V_p}{|I|}, -\Phi_I\right) \quad (72)$$

The use of a.c. polarization with thin-layer electrodes appears to offer the advantage that the rates

of electrode reactions too fast for measurement by d.c. thin-layer voltammetry ($10^{-4} < {}^*k^0 < 1$ cm sec^{-1}) may be measured at the characteristically clean surfaces afforded by such electrodes. Differential double-layer-capacitance data, C, are also obtained, corresponding to various points on the d.c. potential scan.

If the measured impedance, Z, is modeled after the simple RC network shown below,

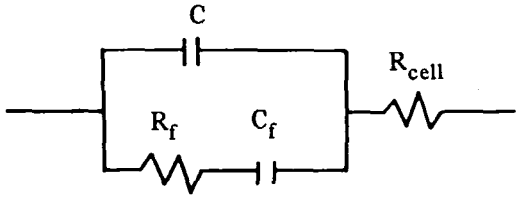

then Z is given by

$$Z = [R_f - j/\omega C_f)^{-1} + j\omega C]^{-1} + R_{cell} \qquad (73)$$

In ideal cases, C and R_{cell} are evaluated from the limiting value (Z_{HF}) that Z attains either at frequencies so high that the faradaic components R_f and C_f are negligible (or in the absence of reactant):

$$Z_{HF} = R_{cell} - \frac{j}{\omega C} \qquad (74)$$

The faradaic impedance component, Z_f, for which the real component equals R_f and the quadrature component equals $1/\omega C_f$, is obtained from the measured impedance, Z, by performing the appropriate vector addition:

$$Z_f \equiv R_f - j/\omega C_f = [(Z - R_{cell})^{-1} - j\omega C]^{-1} \qquad (75)$$

The experimental values of R_f and C_f are related to the rate of the electrode reaction by equations obtained by solving Fick's second law, subject to the boundary condition appropriate to Reaction 1:

$$nFAD_{Ox}\left(\frac{\partial C_{Ox}}{\partial x}\right)_{x=0} = -nFAD_R\left(\frac{\partial C_R}{\partial x}\right)_{x=0} = i + \frac{V_p \sin\omega t}{Z_f} \qquad (76)$$

The result, which applies to plane electrodes of all types including TLE, is[4]

$$C_{Ox}(x,t) = C_{Ox}(x) + \frac{|I|}{nF}\frac{2D_{Ox}}{\omega}^{\frac{1}{2}} \exp\left[-\frac{\omega}{2D_{Ox}}^{\frac{1}{2}} x\right] \times \left\{\sin\omega t - \left(\frac{\omega}{2D_{Ox}}\right)^{\frac{1}{2}} x - \cos\left[\omega t - \left(\frac{\omega}{2D_{Ox}}\right)^{\frac{1}{2}} x\right]\right\} \qquad (77)$$

Combining Equation 77 with the differential equation describing the series RC circuit

$$\frac{dE}{dt} = |I| R_f \omega \cos\omega t + \frac{|I|}{C_f} \sin\omega t \qquad (78)$$

and with the exact derivative expression for a function of variables i, C_{Ox} and C_R

$$\frac{dE}{dt} = \frac{\partial E}{\partial i}\frac{di}{dt} + \frac{\partial E}{\partial C_{Ox}(0)}\frac{dC_{Ox}(0)}{dt} + \frac{\partial E}{\partial C_R(0)}\frac{dC_R(0)}{dt} \qquad (79)$$

leads to general expressions for R_f and C_f in terms of the electrode rate parameters:[14]

$$R_f = \left(\frac{\partial E}{\partial i}\right) + s/\omega^{\frac{1}{2}} \qquad (80)$$

$$C_f = 1/s\omega^{\frac{1}{2}} \qquad (81)$$

$$s \equiv \frac{\sqrt{2}}{2nFA}\left[\frac{1}{D_{Ox}^{\frac{1}{2}}}\frac{\partial E}{\partial C_{Ox}(0)} - \frac{1}{D_R^{\frac{1}{2}}}\frac{\partial E}{\partial C_R(0)}\right]$$

The exact form of Equations 80 and 81 will depend on the electrode rate law that is used to obtain $\partial E/\partial i$, $\partial E/\partial C_{Ox}(0)$ and $\partial E/\partial C_R(0)$ are calculated. For example, if the reaction (Equation 1) follows Equation 14, then Equations 82 to 84 apply:

$$\frac{\partial E}{\partial i} = \frac{-RT}{F}({}^*\alpha i - a^i)^{-1} \qquad (82)$$

$$\frac{\partial E}{\partial C_{Ox}} = \frac{-RT}{F}\frac{c^i}{\overline{C_{Ox}}}\frac{}{{}^*\alpha i - a^i} \qquad (83)$$

$$\frac{\partial E}{\partial C_R} = \frac{RT}{F}\frac{a^i}{\overline{C_R}}\frac{}{{}^*\alpha i - a^i} \qquad (84)$$

where i, c_i and a_i are defined by Equations 14 to 16. The symbols $\overline{C_{Ox}}$ and $\overline{C_R}$ denote the analytical (i.e., nonsinusoidal, average) concentrations of the reactants in the thin-layer cavity. Of particular practical importance is the case in which the d.c. component of the current obeys the Nernst equation ($^*k^0 > 10^{-4}$ cm sec^{-1}), whereas the a.c. component does not ($^*k^0 < 1$ cm sec^{-1}); then $\overline{C_{Ox}}$ and $\overline{C_R}$ follow the Nernst equation in a form analogous to Equation 8:

$$\overline{C_{Ox}} = C^0\left\{\exp\left[\frac{-nF}{RT}(E - E^0)\right] + 1\right\}^{-1} \qquad (85)$$

where, by analogy with Equation 9:

$$C^0 = \overline{C_{Ox}} + \overline{C_R} \tag{86}$$

Thus, $*a$ and $*k^0$ can be determined from t, even when the reaction is too fast for measurement by d.c. polarization alone, by means of the following steps. The value of Z is corrected for the influence of R_{cell} and C by means of Equation 75, giving Z_f; the quantities given by Equations 82 to 86 are inserted into Equations 80 and 81, as appropriate, and the numerical values of $*a$ and $*k^0$ are extracted from the resulting expression. A graph of the faradaic current amplitude, $|I_f|$, calculated by means of Equations 80 to 87 appears in Figure 5.

$$|I_f| = \frac{V_p}{(R_f^2 + 1/\omega^2 C_f^2)^{1/2}} \tag{87}$$

The potential E^0 at which the d.c. component achieves its peak value i_p is a mathematically convenient point at which to evaluate $*k^0$:

$$R_f(E=E^0) = \frac{2RT}{nF^2AC^0}\frac{1}{*k^0}\frac{(2/\omega)^{1/2}}{C^0}\frac{RT}{F}\left[\frac{1}{D_{Ox}^{1/2}} + \frac{1}{D_R^{1/2}}\right] \tag{88}$$

Equation 88 can then be used to evaluate $*a$, employing this value of $*k^0$, at some other potential $E \neq E^0$; for instance, if $E \ll E^0$, so that $i_a \ll i_c$, then:

$$R_{f(E<<E^0)} = \frac{-RT}{nFC^0}\frac{1}{*\alpha}\left\{\frac{1}{FA\ *k^0\ \exp\left[\frac{-*\alpha F}{RT}(E-E^0)\right]}\right.$$
$$\left. - \frac{1}{(2\omega)^{1/2}FA}\left[\frac{1}{D_{Ox}^{1/2}} + \frac{1}{D_R^{1/2}}\exp\left(\frac{F}{RT}(E-E^0)\right)\right]\right\} \tag{89}$$

From Equation 88 it can be seen that the accuracy with which $*k^0$ can be determined increases with increasing angular frequency, ω, and initial reactant concentration, C^0. The upper limit of frequency is imposed by the presence of the double-layer capacitance, C, which is in parallel with the faradaic impedance and acts to shunt the applied current at high frequencies. The practical limits appear to be about $*k^0 \leqslant 1$ cm sec^{-1} and $\omega \leqslant 10^6$ rad sec^{-1}.

E. Steady-State Amperometry[15,16]

It is possible to envision situations in which thin-layer amperometry may be the preferred technique, either because of its insensitivity to double-layer charging currents or because

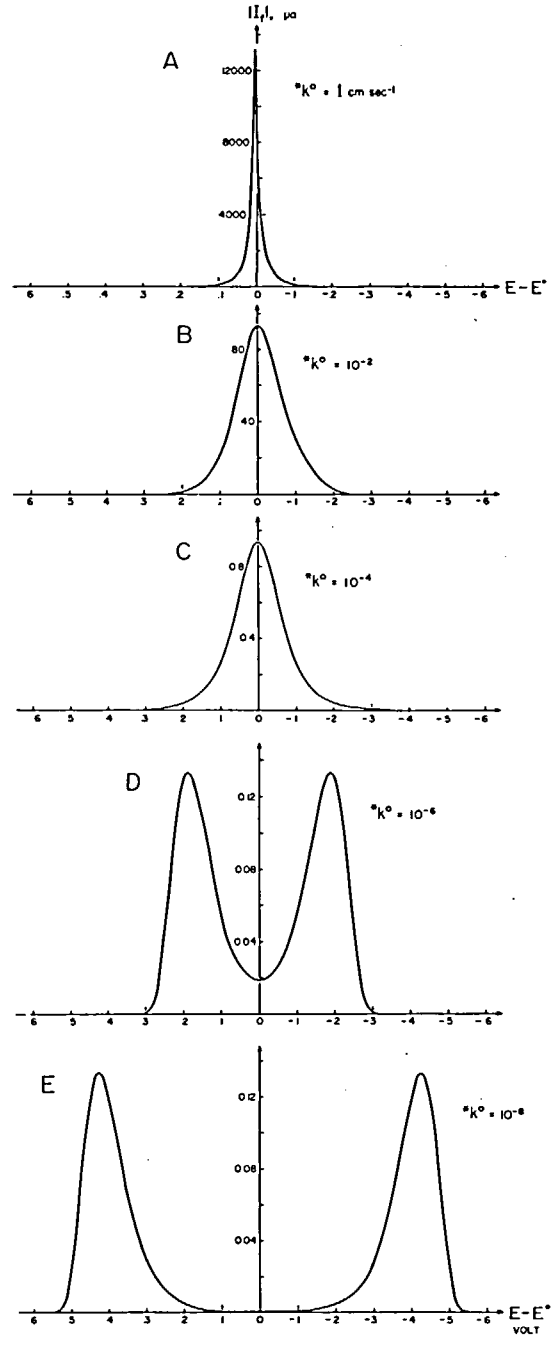

FIGURE 5. Theoretical thin-layer alternating current-potential curves.[37] Graph of $|I_f|$ from Equations 80 to 87 for the following values of the parameters: A = 1 cm^2, $*a$ = 0.50, $C^0 = 10^{-3}$ F, $D_{Ox} = D_R = 10^{-5}$ cm^2 sec^{-1}, n = 1, T = 300°K, V_p = 5 mV, and $\omega/2\pi = 10^3$ Hz. Curve A. $*k^0 \geqslant 1$ cm sec^{-1} (reversible a.c., d.c. response); Curve B. $*k^0 = 10^{-2}$ m sec^{-1} (a.c. irreversible; d.c. reversible); Curve C. $*k^0 = 10^{-4}$ cm sec^{-1} (a.c. irreversible; d.c. reversible); Curve D. $*k^0 = 10^{-6}$ cm sec^{-1} (irreversible a.c., d.c. response); Curve E. $*k^0 = 10^{-8}$ cm sec^{-1} (irreversible a.c., d.c. response).

especially accurate values of diffusion coefficients are wanted. The theory and practice of steady-state amperometry with thin-layer electrodes have been described by Reilley and co-workers.[15-17]

1. Reversible Reactions (Four-electrode Cells)

One particularly versatile approach uses a cell equipped with two parallel or concentric electrode surfaces separated by a thin layer of solution, such as the micrometer TLE design described in Part III, Section A, the potentials of the two surfaces being adjusted independently by means of auxiliary- and reference-electrode circuitry. It is convenient to fix the potential of one electrode surface such that oxidation (or reduction) of reactant arriving at that face occurs at a diffusion-limited rate. The potential of the opposing electrode surface is then adjusted so that reduction (or oxidation) commences and electrolysis is continued until a steady-state current is achieved. If the reaction (Equation 1) obeys the Nernst equation (Equation 6), the current follows Equations 90 and 91:

$$i_c = \frac{2nFAD_R C^0}{\ell\left\{1 + \frac{D_R}{D_{Ox}} + 2\exp\left[\frac{nF}{RT}(E-E^0)\right]\right\}} \quad \text{(reduction)} \tag{90}$$

$$i_a = -\frac{2nFAD_{Ox} C^0}{\ell\left\{1 + \frac{D_{Ox}}{D_R} + 2\exp\left[-\frac{nF}{RT}(E-E^0)\right]\right\}} \quad \text{(oxidation)} \tag{91}$$

where A is the *cross-sectional* area of the electrode cavity. The limiting current, i_L, is given by Equation 92:

$$i_L = \pm\frac{2nFAC^0}{\ell}\frac{D_{Ox}D_R}{D_{Ox} + D_R} \tag{92}$$

The potential $E_{1/2}$ at which $i = i_L/2$ is given by

$$E_{1/2} = E^0 + \frac{RT}{nF}\ln\left[\frac{(1 + D_R/D_{Ox})}{2}\right] \quad \text{(reduction)} \tag{93}$$

$$E_{1/2} = E^0 + \frac{RT}{nF}\ln\left[\frac{(1 + D_{Ox}/D_R)}{2}\right] \quad \text{(oxidation)} \tag{94}$$

A graph of Equation 90 appears in Figure 6.

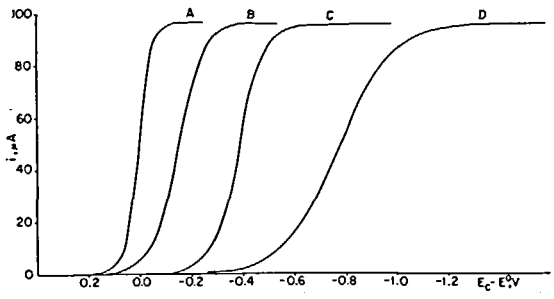

FIGURE 6. Theoretical cathodic thin-layer four-electrode steady-state amperometric curves. Graphs of Equations 90 and 105 for the following values of the experimental parameters: Curve A. reversible reaction; Curve B. $*\alpha = 0.50$, $*k^0 = 10^{-3}$ cm sec^{-1}; Curve C. $*\alpha = 0.50$, $*k^0 = 10^{-6}$ cm sec^{-1}; and Curve D. $*\alpha = 0.25$, $*k^0 = 10^{-6}$ cm sec^{-1}. $A = 0.50$ cm^2, $C^0 = 10^{-3}$ F, $D_{Ox} = D_R = 10^{-5}$ cm^2 sec^{-1}, $\ell = 5 \times 10^{-3}$ cm, and T = 298°K. (Reprinted from Reference 1 by courtesy of Marcel Dekker, Inc.)

Equations 90 to 94 were obtained as follows: Under steady-state conditions, Fick's second law of diffusion, Equation 5, takes the form

$$\frac{\partial C_{Ox}}{\partial t} = D_{Ox}\frac{\partial^2 C_{Ox}}{\partial x^2} = 0 \tag{95}$$

which on integration yields

$$D_{Ox}\left(\frac{\partial C_{Ox}}{\partial x}\right)_{x=0} = \frac{D_{Ox}}{\ell}[C^0 - C_{Ox}(x=0)] \tag{96}$$

The current is given by

$$i = \frac{nFAD_{Ox}}{\ell}[C_{Ox}(x=\ell) - C_{Ox}(x=0)] \tag{97}$$

Equations for the oxidation process can be written similarly. Since the quantity of reactant in the solution is constant, it is clear that

$$C^0 = \frac{C_{Ox}(x=\ell) + C_{Ox}(x=0) + C_R(x=\ell)}{2} \tag{98}$$

where C_{Ox} (x=0) and C_R (x=0) obey the Nernst equation:

$$E = E^0 + \frac{RT}{nF}\ln\frac{C_{Ox}(x=0)}{C_R(x=0)} \tag{99}$$

Solving Equations 98 and 99 for $[C_{Ox}^{(x=\ell)} - C_{Ox}(x=0)]$ and substituting the result into Equation 97 gives the desired result, Equation 90.

2. Time Required to Reach Steady-state Conditions in Thin-layer Amperometry

The time required to reach steady-state conditions within a fraction, ϵ, of the current can be estimated from the appropriate time-dependent solution of the diffusion equation, which is[4]

$$C_{Ox}(x,t) = C_{Ox}(0,t) + [C_{Ox}(\ell,t) - C_{Ox}(0,t)]\frac{x}{\ell} + \frac{2}{\pi}\sum_{m=1}^{\infty}\frac{1}{m}\left\{C_{Ox}(\ell,t)(-1)^m - C_{Ox}(0,t) + C^0[1-(-1)^m]\right\} \times \sin\left(\frac{m\pi x}{\ell}\right)\exp\left[-\frac{m^2\pi^2 D_{Ox}t}{\ell^2}\right] \quad (100)$$

Substitution of $C_{Ox}(x, t)$ from Equation 100 into Equation 101

$$c^i(t) = nFAD_{Ox}\left(\frac{\partial C_{Ox}}{\partial x}\right)_{x=0} \quad (101)$$

leads to an expression for the time-dependent current:

$$c^i(t) = \frac{nFD_{Ox}}{\ell}[C_{Ox(\ell,t)} - C_{Ox(0,t)}] + \frac{2nFD_{Ox}}{\ell}\sum_{m=1}^{\infty}\left\{C_{Ox(\ell,t)}(-1)^m - C_{Ox(0,t)} + C^0[1-(-1)^m]\right\}\exp\left[-\frac{m^2\pi^2 D_{Ox}t}{\ell^2}\right] \quad (102)$$

Comparing the right-hand side of Equation 102 with that of Equation 97 reveals that $i_c(t)$ is equal to the steady-state current within a relative error less than ϵ when the time-dependent terms of Equation 102 meet the condition represented by Equation 103:

$$\sum_{m=1}^{\infty}\left\{C_{Ox}(\ell,t)(-1)^m - C_{Ox}(0,t) + C^0\left[1-(-1)^m\right]\right\} \times \exp\left[-\frac{m^2\pi^2 D_{Ox}t}{\ell^2}\right] < \epsilon[C_{Ox}(\ell,t) - C_{Ox}(0,t)] \quad (103)$$

Terms for which $m > 1$ can be neglected. Solving for t gives

$$t \geq \frac{\ell^2}{\pi^2 D_{Ox}}\ln\frac{1}{\epsilon} \quad (104)$$

For example, if $D_{Ox} = 10^{-5}$ cm^2 sec^{-1} and $\ell = 10^{-3}$ cm, then 0.05 sec is required to reach steady-state conditions within a relative error $\epsilon = 0.01$ (1%).

3. Irreversible Reactions (Four-electrode Cells)

In the event that the electrode reaction (Equation 1) exhibits irreversible behavior (Equation 15), the steady-state current can be found by combining Equations 97, 15, and 98:

$$c^i = \frac{2nFAD_R C^0}{\ell(1+D_{Ox}/D_R)+2\ell\exp[(nF/RT)(E-E^0)]+(2D_R/{}^*k^0)\exp[{}^*\alpha F/RT)(E-E^0)]} \quad (105)$$

This equation implies that the reoxidation of species R is diffusion-controlled at the surface having the more positive potential. A graph of Equation 105 appears in Figure 6. Similarly, for irreversible oxidation:

$$a^i = \frac{2nFAD_{Ox}C^0}{\ell(1+D_R/D_{Ox})+2\ell\exp[(nF/RT)(E-E^0)]+(2D_{Ox}/{}^*k^0)\exp[-(1-{}^*\alpha)(F/RT)(E-E^0)]} \quad (106)$$

In order to extract numerical values of $^*\alpha$ and $^*k^0$ from experimental data, a graphical procedure is used. Equation 105 may be rewritten in the form

$$\ln\left\{\frac{2nFAC^0}{c^i} - \frac{\ell}{D_R + D_{Ox}} - \frac{\ell}{D_R}\exp\left[\frac{F}{RT}(E - E^0)\right]\right\} = \frac{{}^*\alpha F}{RT}(E - E^0) - \ln {}^*k^0 \quad (107)$$

A plot of the left-hand side of Equation 107 against $E-E^0$ is linear and has a slope equal to $^*\alpha F/RT$ and an intercept (at $E=E^0$) equal to $-\ln {}^*k^0$.

4. Reversible Reactions (Two-electrode Cells)

When a voltage is applied between opposing faces of a two-electrode thin-layer cell, there is no

flow of current, apart from that due to background reactions, unless both the oxidized form and the reduced form of the reactant are present initially. If the electrode reaction obeys the Nernst equation, the steady-state current follows Equation 108:

$$\Delta E = \frac{RT}{nF} \ln \frac{(C^0_{Ox} + J)[C^0_R + (D_{Ox}/D_R)J]}{(C^0_{Ox} - J)[C^0_R - (D_{Ox}/D_R)J]} \quad (108)$$

where ΔE is the voltage between the electrodes and $J = i\ell/(2nF A D_{Ox})$. A graph of Equation 108 appears in Figure 7. The limiting current, i_L, is given by Equations 109 or 110, whichever predicts the smaller value.

$$i_L = \frac{2nFAD_R C^0_R}{\ell} \quad (109)$$

$$i_L = \frac{2nFAD_{Ox} C^0_{Ox}}{\ell} \quad (110)$$

Equation 108 was derived from the time-independent form of Fick's second law, Equation 95, applied to both surfaces of the thin layer cell:

$$D_{Ox} \frac{\partial C_{Ox}}{\partial x} = -D_R \frac{\partial C_R}{\partial x} = \frac{D_{Ox}}{\ell} [C_{Ox}(x=\ell) - C_{Ox}(x=0)]$$
$$= \frac{D_R}{\ell} [C_R(x=0) - C_R(x=\ell)] \quad (111)$$

The current is given by

$$i = \frac{nFAD_{Ox}}{\ell} [C_{Ox}(x=\ell) - C_{Ox}(x=0)]$$
$$= \frac{nFAD_R}{\ell} [C_R(x=0) - C_R(x=\ell)] \quad (112)$$

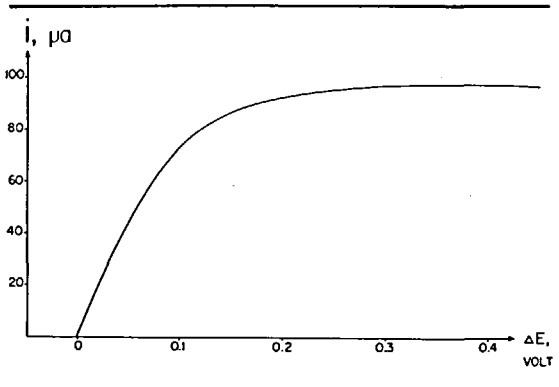

FIGURE 7. Theoretical thin-layer two-electrode current-voltage curve for a reversible reaction. Graph of Equation 108 for the following values of the experimental parameters: $A = 0.5$ cm^2, $C^0_{Ox} = C^0_R = 5 \times 10^{-3}$ F, $D_{Ox} = D_R = 10^{-5}$ cm^2 sec^{-1}, $\ell = 5 \times 10^{-3}$ cm, $n = 1$, and $T = 298$°K. (Reprinted from Reference 1 by courtesy of Marcel Dekker, Inc.)

Equation 112 can be solved for the individual surface concentrations by noting that no net change of valence state occurs during the experiment (Equations 113 and 114):

$$C^0_{Ox} = [C_{Ox}(x=\ell) + C_{Ox}(x=0)]/2 \quad (113)$$

$$C^0_R = [C_R(x=\ell) + C_R(x=0)]/2 \quad (114)$$

Substituting the results into the Nernst equation, written for the two surfaces of the thin-layer cell,

$$\Delta E = \frac{RT}{nF} \ln \frac{C_{Ox}(x=\ell)\, C_R(x=0)}{C_{Ox}(x=0)\, C_R(x=\ell)} \quad (115)$$

yields the desired result, Equation 108.

F. Definitions of Symbols

A = electrode area, cm^2

A = cross-sectional area of thin-layer electrode cavity, cm^2

α = charge-transfer coefficient, corrected for diffuse double layer dependence

$^*\alpha$ = observed value of charge-transfer coefficient

C = differential capacitance of electrode-solution interface, farad cm^{-2}

C^0 = initial concentration of reactant, mole cm^{-3}

$_iC_b$ = bulk concentration of ith species, mole cm^{-3}

C_d = component of differential capacitance due to diffuse layer, farad cm^{-2}

C_f = faradaic component of electrode capacitance, farad cm^{-2}

C_{Ox} = concentration of reactant in oxidized form, mole cm^{-3}

C_R = concentration of reactant in reduced form, mole cm^{-3}

D = diffusion coefficient (also D_{Ox}, D_R), cm^2 sec^{-1}

E = electrode potential relative to a reference electrode, volts

$E(0)$ = starting electrode potential, volts

E^0 = formal (reduction) potential, volts

E_p = potential at a voltammetric peak, volts

$_cE_p$, $_aE_p$ = potential at a voltammetric peak for cathodic or anodic scan, volts

E_z = potential at which electrode electronic charge is zero, volts

ΔE = voltage between electrodes in two-electrode amperometry, volts

e = 2.718...

ϵ = relative error, $\Delta x/x$

F = Faraday constant; coul equiv^{-1}

Γ = interfacial excess, mole cm^{-2}

I = a.c. component in a.c. voltammetry, amp

I_f = faradaic a.c. component, amp

i = d.c. current component, amp

$_a i$, $_c i$ = anodic or cathodic d.c. component, amp

i_L = steady-state limiting current in amperometry, amp

i_p = peak current, amp

$_a i_p$, $_c i_p$ = peak current observed with anodic or cathodic potential scan, amp

$j = (-1)^{1/2}$

k^0 = standard electrochemical rate constant, corrected for diffuse-layer dependence, cm sec^{-1}

$^*k^0$ = apparent standard electrochemical rate constant, cm sec^{-1}

ℓ = thickness of solution in a direction normal to the electrode surface, cm

n = net number of electrons transferred per molecule of reactant

$_i\phi_2$ = potential at outer Helmholtz plane in i^{th} species (such as Ox or R), volts

Q = net charge transferred, coul

Q_b = net charge transferred due to background reaction, coul

R = ideal gas constant, joule mole^{-1} °K^{-1}

R_f = faradaic component of electrode resistance, ohms

R_{cell} = component of cell impedance due to solution resistance, ohms

T = temperature, °K

t = time, sec

τ = chronopotentiometric transition time, sec

τ_b = chronopotentiometric transition time due to background reactions, sec

V = volume of solution, cm^3

V_p = peak voltage of a.c. signal, volts

x = distance from an electrode surface, cm

Z = impedance of electrode, ohms

Z_f = faradaic component of electrode impedance, ohms

Z_i = ionic charge of i^{th} ionic species (such as Ox or R)

ω = angular frequency of a.c. signal, radian sec^{-1}

III. APPARATUS

A. Thin-layer Electrodes

Numerous thin-layer electrode designs have been developed for general use,[18-24] for use with commercial spectrometers,[25-27] for continuous flow of reactant through the thin-layer cavity,[28-31] for minimal ohmic polarization in poorly conducting electrolytes,[12] and for studies requiring a pure mercury electrode surface.[32] Several particularly effective designs are described in the following sections.

1. Thin-layer Electrodes for General Use

The TLE design most frequently used in the author's laboratory is shown in Figure 8. A section of precision-bore, heavy-wall Pyrex® tubing (Wilmad Glass Co., Buena, N.J. 08130) is cut to the appropriate size (0.1235 ± 0.0002 in. I.D. x 9 mm O.D. x 11 mm length) by means of a wet-wheel saw, care being taken to produce true, carefully finished ends. The precision-bore tubing is sealed to a length of standard-wall tubing of slightly larger (10-mm) outside diameter (10 mm O.D.), the heat of the sealing flame being directed primarily against the nonprecision tubing to avoid distortion of the precision bore. For this purpose it is convenient to mount the sections of tubing firmly on a ring-stand by means of buret clamps and a length of graphite rod. A strip of 1/8 in. polished Pyrex plate is then sealed over the open end of the precision-bore tubing to form a cap, care taken not to melt or otherwise distort the precision bore. By using the side of the wet-wheel saw, the cap is ground at 45° angles on opposite sides until application of gentle pressure causes fluid to flow past the cap; this is necessary in order to provide sufficient contact of solution with the thin-layer cavity while avoiding direct exposure of the electrode to the solution outside the cavity. A rod-shaped piece of electrode material is fabricated

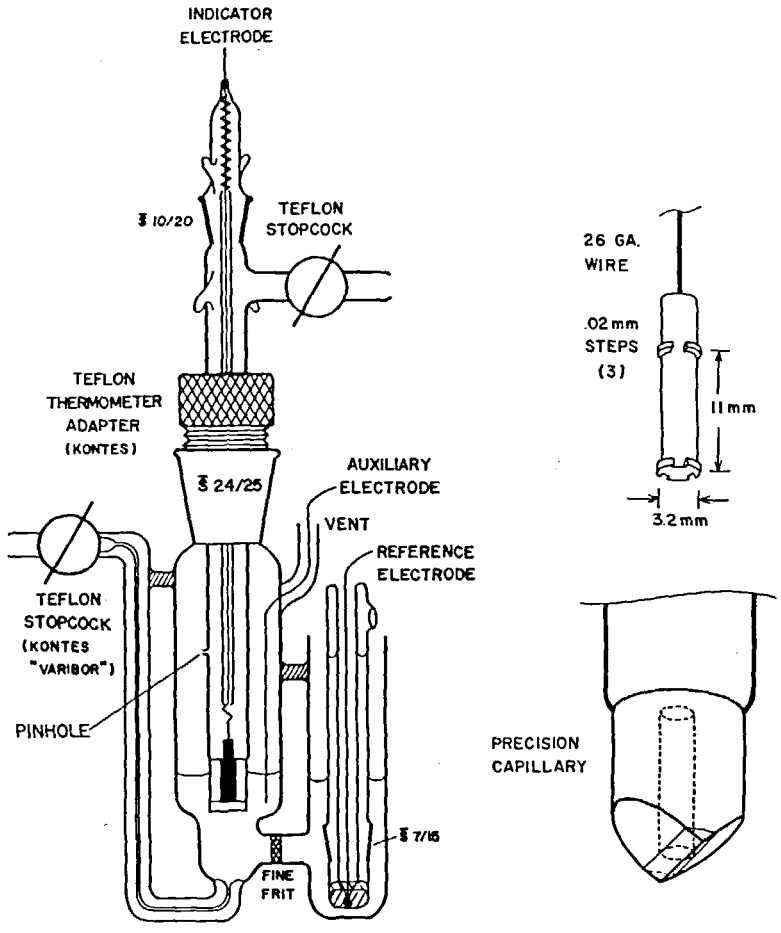

FIGURE 8. Immersible thin-layer electrode and H-cell.[6,33]

by appropriate conventional machining techniques. Rings on each end of the electrode rod, notched to provide a path for solution flow, are fitted to the diameter of the precision-bore tubing to insure uniform positioning within the cavity. The final spacing, ℓ, between the surface of the electrode and the glass wall is about 2×10^{-3} cm. The electrode is held in place by a spring-loaded glass tube and can be removed for cleaning. Pure metals suitable for construction of TLE can be obtained from the Materials Research Corporation, Orangeburg, N.Y. 10962, Engelhard Industries, Inc., Carteret, N.J. 07008, and Matthey-Bishop, Inc., Malvern, Pa. 19355.

When in use, the thin-layer cell is inserted into the H-cell so that the tip is slightly below the surface of the reactant solution, filling the cavity by capillary action. Spent solution is removed from the cavity by applying an inert gas under pressure; this must generally be repeated about ten times to insure complete renewal of the solution layer.[22] The volume of the cavity may be evaluated coulometrically, using 10.00 mF Fe(III) in 1 F perchloric acid. From such calibration data, it is apparent that the precision of electrodes of this design is limited primarily by the degree to which the surface state can be reproduced in successive experiments, rather than by mechanical factors such as the reproducibility of the volume of solution in the thin-layer cavity.[1,6,22] A precision of ± 1% is typical for well-behaved systems.

A cell of this design, constructed of fused quartz, has been employed to study solutions in molten salts.[33] Figure 9 is a diagram of the apparatus used to heat the melt and maintain an inert atmosphere. A two-compartment crucible was employed; one compartment contained the

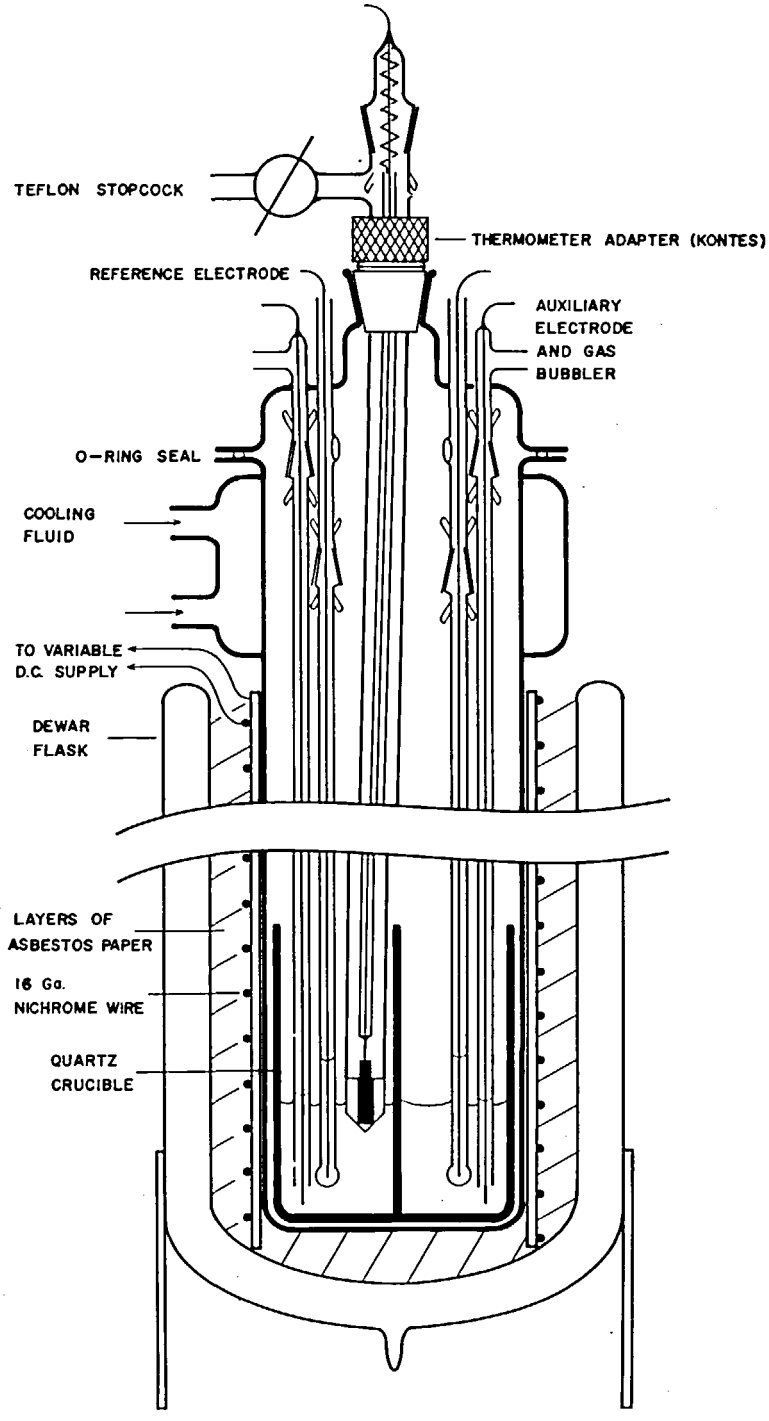

FIGURE 9. Oven and container for thin-layer electrochemistry in molten salts.[33]

pure melt and the other the reactant solution, permitting frequent checking of the background current. Transfer of the thin-layer electrode between compartments was accomplished without significant cross-contamination. Each compartment contained a reference electrode and a small tube which served both to introduce a stream of inert gas and as a guide for the auxiliary electrode, a 26-gauge platinum wire. The thin-layer electrode was introduced into the inert atmosphere through a Kontes Teflon® thermometer adapter, which maintained an airtight seal, but allowed the electrode to be transferred from one compartment of the crucible to the other. The temperature of the melt was controlled manually by means of a variable transformer, the output of which was rectified and passed through a π-section filter to prevent the introduction of electronic noise into the electrochemical circuit by the field in the coils of the resistance-heated oven. The temperature was constant within the limits of sensitivity of the mercury or gallium thermometer (about ± 2°C).

It is not absolutely necessary to calibrate a newly constructed cell in a standard melt because the volume of the cavity can be determined by measuring its dimensions directly. The volume decreases with increasing melt temperature, for the thermal expansion of the electrode is greater than that of glass, but this effect is described with an accuracy sufficient for analytical purposes (Table 1), by Equation 116:

$$V = V^0 - \pi D^0 h K (T - T^0) \qquad (116)$$

where V^0 is the cell volume and D^0 is the electrode diameter at a reference temperature, T^0; h is the height of the solution layer, and K is the thermal coefficient of expansion of the electrode material. The change in solution layer thickness is not so large as to cause departure from the thin-layer electrode equations; for example, the 3-mm diameter of a platinum electrode changes by only about 0.02 mm upon going from 25 to 450°C.

The application of thin-layer techniques to the study of molten salts is discussed further in Part IV, Section G.

Thin-layer electrodes of the micrometer type, though more difficult to construct and use than those of the capillary design, have very often been used in the development of new thin-layer

TABLE 1

Thin-layer Coulometry of Cr(III) in LiCl-KCl Eutectic Melt[33]

Trial	T, °K	C^O, m*F*	Q, mcoul	Q_b, mcoul	V x 10^3, from Eq. 116, cm^3	V x 10^3, cm^3
1	298[a]	9.948	5.783	0.0918	5.93[b]	5.93 ± .05
2	641	5.710	3.164	0.214	5.39	5.35
3	669	5.661	3.100	0.170	5.35	5.36 ± 0.4[c]
4	719	5.572	3.157	0.318	5.28	5.28
5	754	5.510	2.953	0.316	5.21	4.96

Experimental conditions: The melt contained $CrCl_3$, LiCl, and 51% KCl, and the electrode area was 1.15 cm^2.

The initial and final potentials were

Trial	$E_{initial}$, V	E_{final}, V	Reference electrode
1	+0.70	+0.35	N.C.E.
2	+0.45	−0.15	Ag/0.05 *F* AgCl in LiCl-KCl eutectic
3	+0.50	−0.15	do.
4	+0.54	−0.20	do.
5	+0.60	0.00	do.

Notes: (a) Average of 5 trials with $Fe(ClO_4)_3$ in 1 *F* $HClO_4$, (b) Reference temperature, (c) Average of 6 trials.

techniques[1,3,12,15-19,21,23,34] and have been preferred for thin-layer amperometry.[17] Several micrometer-electrode designs have been described;[18-21] one of them[17] is illustrated in Figure 10. Rods 6 mm in diameter and 10 mm long, carefully machined from the electrode material, were cemented to the spindle and anvil of the micrometer (metric micrometer caliper with removable anvil, Model No. 2 MARL, L. S. Starrett Co., Athol, Mass. 01331) by way of Plexiglas® discs that served to insulate the electrodes from the micrometer. Teflon sleeves were used to protect the cemented connection from the electrolyte, and the micrometer was coated with a chemical-resistant paint. Electrical connections were established by means of wire contacts, formed from the electrode metal, held in place by elastic bands.

When in use, the electrode was clamped in a vertical position with the micrometer head uppermost. The electrode faces were positioned several millimeters apart and rinsed with reactant solution contained in a reservoir such as that shown in Figure 10. Closing the gap to about 4 x 10^{-3} cm caused the excess liquid to flow down the side of the lower electrode and out of contact with the thin layer of solution, after which it was removed with a dropper. An edge of the solution layer was then positioned against the tip of the contact arm and the cell was ready for use.

Careful exclusion of the atmosphere is important for most applications and was accomplished by placing the electrode within a transparent polyethylene glove, supplied with pressurized nitrogen. The fingers of the glove served as convenient entrance ports for the nitrogen, electrode leads, contact arm, reactant solution, and micrometer head. A cover and solution reservoir have been described[19] which appear to offer the advantage of convenience and decreased

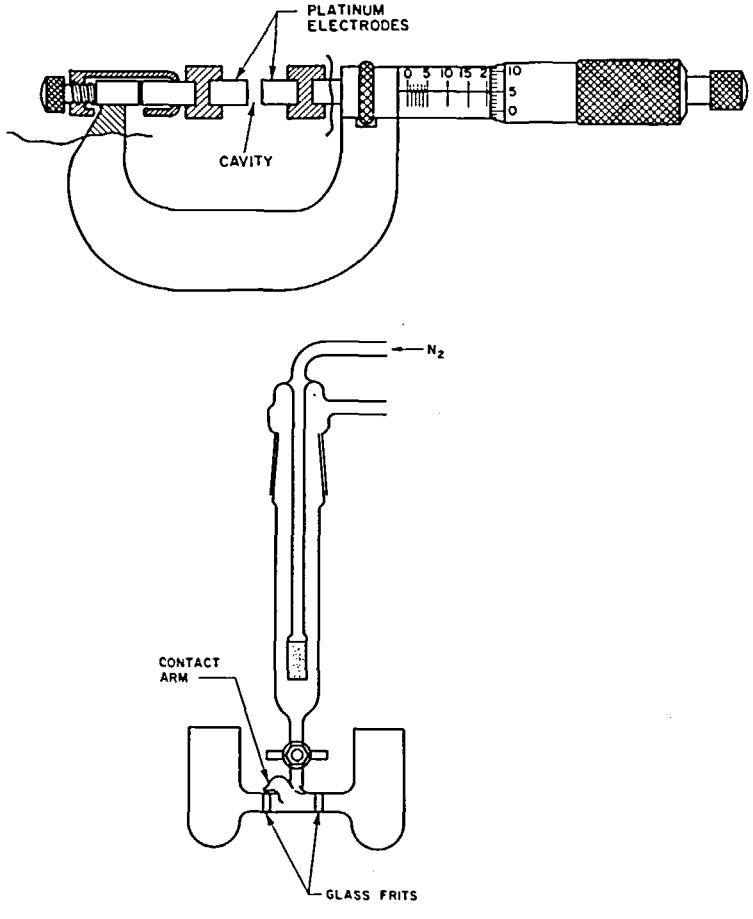

FIGURE 10. Micrometer thin-layer electrode and H-cell. (Reprinted from Reference 18 by courtesy of the American Chemical Society.)

cell resistance, at the expense of increased diffusion of reactant between the cavity and the surrounding solution.

Tests of the precision obtainable with micrometer thin-layer electrodes are reported in References 18 to 21. Although a mechanical reproducibility of ± 1% is typical, the precision observed in practical applications is usually limited by the reproducibility of the electrode surface state, and is particularly likely to be so limited at reactant concentrations below 10^{-3} *F*. The rate of loss of 0.1 *F* Fe(III) in 1 *F* $HClO_4$ from the cavity into a contact arm containing 1 *F* $HClO_4$ was measured and found to be about 2% in 60 min.[18] Care must be taken, however, to insure that the electrolyte in the contact arm is less dense than the reactant solution in the thin-layer cavity, preventing convective mixing of the two solutions.

2. Thin-layer Electrodes for Use with Poorly Conducting Electrolytes

Charge flowing between the auxiliary electrode and thin-layer electrolytes follows a relatively tortuous path along the length of the solution layer, as illustrated for the micrometer electrode in Figure 11. Charge flowing from the capillary (contact arm) to a nearby point, A, encounters less total resistance than that flowing to a more distant point, B. Accordingly, the current density is greater and the consumption of reactant faster at A than at B, so that the effective length of the current path increases during the experiment. The resulting ohmic polarization of the solution layer is negligible for 10^{-3} *F* reactants in the presence of 1 *F* supporting electrolyte; however, it becomes a serious problem at higher reactant concentrations or with more dilute supporting electrolytes. Furthermore, since the current density and surface concentration display complicated time-dependences whose characteristics vary with each individual electrode reaction, it is a complicated matter to compensate for the resulting ohmic polarization by electronic feedback or to correct for its effects through processing of the data, although procedures applicable to some cases have been devised.[35,36]

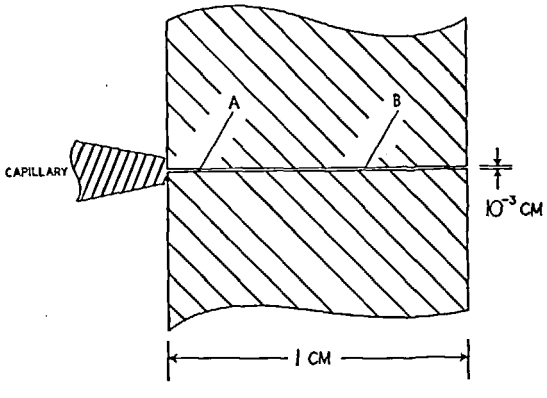

FIGURE 11. Schematic diagram of micrometer electrode. (Reprinted from Reference 12 by courtesy of the American Chemical Society.)

The effects of ohmic polarization on thin-layer electrode behavior are illustrated by the data of Figures 12 to 14. Under experimental conditions entailing large current densities, the peak current in linear potential-scan voltammetry remains below the expected value and is shifted to less

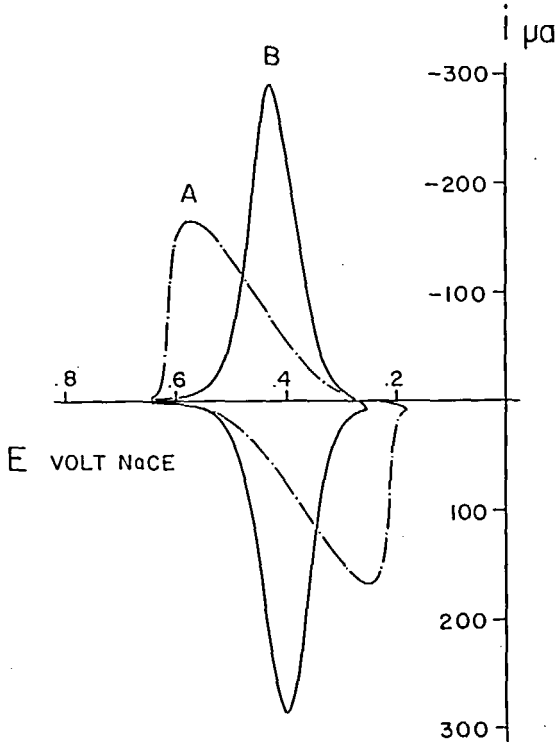

FIGURE 12. Thin-layer cyclic current-potential curves for Fe(III)-Fe(II) at conventional and porous-boundary electrodes. Curve A. Micrometer electrode (Figure 10) Curve B. Porous-boundary micrometer electrode (Figure 16). Experimental conditions: the solution contained 0.1 *F* $Fe(ClO_4)_3$ and 1 *F* $HClO_4$, $\ell = 4.57 \times 10^{-3}$ cm, r = 2 mV sec^{-1}, T = 296 ± 2°K, and V = 1.628×10^{-3} cm^3. A calomel reference electrode (NaCE) prepared with 1 *N* NaCl was employed. (Reprinted from Reference 12 by courtesy of the American Chemical Society.)

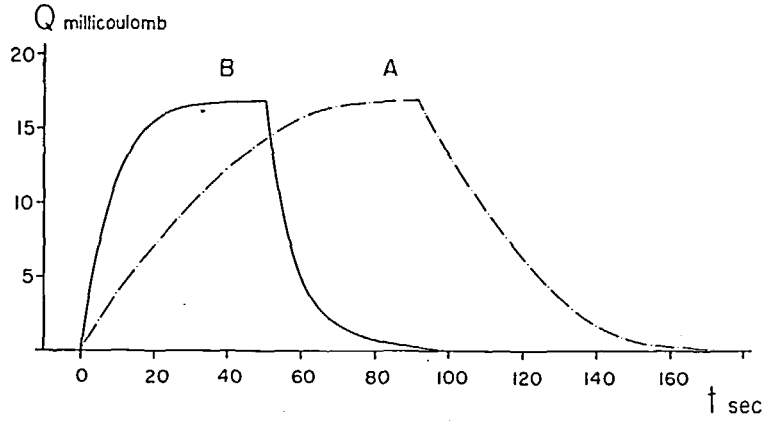

FIGURE 13. Thin-layer potential-step coulometric charge-time curves for conventional and porous-boundary electrodes. Curve A. Micrometer electrode (Figure 10) and Curve B. Porous-boundary micrometer electrode (Figure 16). The initial and final potentials were 0.650 and 0.250 V vs. the calomel reference electrode, respectively. Other conditions were as in Figure 12. (Reprinted from Reference 10 by courtesy of the American Chemical Society.)

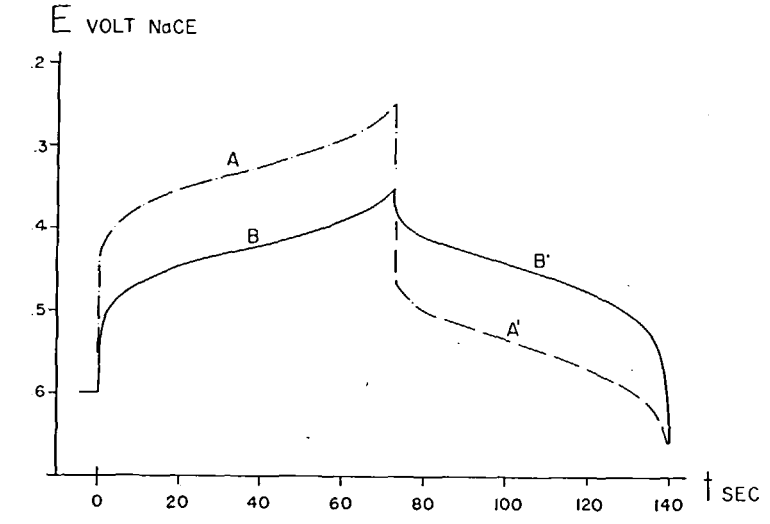

FIGURE 14. Thin-layer chronopotentiometric curves for Fe(III)-Fe(II) at conventional and porous-boundary electrodes. Curve A. Conventional micrometer electrode (Figure 10) and Curve B. Porous-boundary micrometer electrode (Figure 16). Experimental conditions: i = 200 μa; other conditions were as in Figure 12. "NaCE" denotes the calomel reference electrode prepared with 1 *F* NaCl. (Reprinted from Reference 12 by courtesy of the American Chemical Society.)

reversible potentials (Figure 12, curve A). In coulometry the time required to complete the electrolysis is increased by ohmic polarization (Figure 13, curve A), although the accuracy is generally unaffected. Chronopotentiometric potential-time curves are shifted toward less reversible potentials with possible obliteration of the potential-break characteristic of the transition time (Figure 14, curve A). The time required for the establishment of steady-state conditions in four-electrode thin-layer amperometric experiments is increased to about the same extent as in thin-layer coulometry; however, the two-electrode thin-layer amperometric method is virtually impervious to ohmic polarization effects because the flow of current is entirely between the

opposing thin-layer electrode faces through the relatively small resistance afforded by the thin layer of solution.

Direct and virtually complete elimination of ohmic polarization is accomplished by means of "porous-boundary" TLE designs, illustrated schematically in Figure 15. One of the parallel boundaries of the solution layer is constructed of a semiporous or perforated material and the auxiliary electrode is positioned so that the current path from the auxiliary electrode to the surface of the thin-layer electrode passes perpendicularly through the porous boundary; the reference electrode, on the other hand, is connected to the cavity by means of the capillary (contact arm) as before. Thus, the resistance common to the solution paths connecting the auxiliary and reference electrodes to the surface of the thin-layer electrode is merely that across the solution-layer thickness, ℓ, rather than along the length of the layer as in conventional TLE:

$$\text{Resistance} = \frac{\ell}{A} \times \text{resistivity} \qquad (117)$$

For example, if $\ell = 10^{-3}$ cm and A = 1 cm^2, the cell constant, ℓ/A, is 10^{-3} cm^{-1}, compared to 10^3 cm^{-1} for conventional thin-layer cells. Improvement by a factor as large as 10^6 is therefore possible.

The degree of perforation of the porous boundary can always be made small enough to render adsorption and spontaneous diffusion negligible (free area less than 0.01% of the cross-sectional area of the boundary), for it is the smallness and uniformity of the average spacing of the holes, and not their total area, that controls their effectiveness.

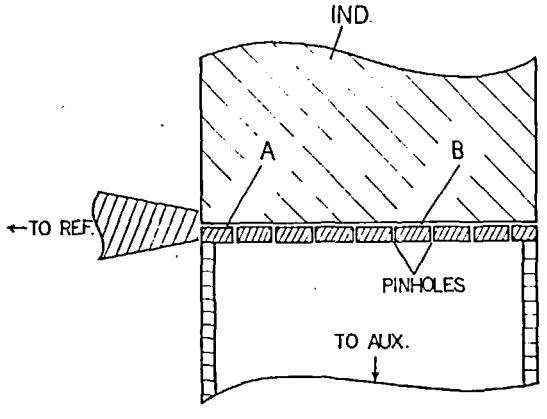

FIGURE 15. Schematic diagram of porous-boundary micrometer electrode solution-cavity. (Reprinted from Reference 12 by courtesy of the American Chemical Society.)

A micrometer-based porous boundary electrode design is shown in Figure 16. A stainless-steel micrometer head (Model No. T1263RL, L. S. Starrett Co., Athol, Mass. 01331) was mounted on a simple aluminum frame; attachment of the platinum rod to the micrometer spindle followed the procedure used for conventional micrometer electrodes (see above). Care was taken to prevent loss of reactant from the thin-layer cavity: The auxiliary electrode compartment was constructed from 1-mm heavy-wall capillary tubing and had a total volume of about 0.05 ml, so that changes in the volume of solution due to normal fluctuations of temperature were negligible. The use of a mercury-mercurous sulfate electrode as the auxiliary electrode avoided bubble formation under conditions of rapid electrolysis. The platinum spinnerette used as the porous boundary was obtained at nominal cost from the Spinnerette Division, Engelhard Industries, Inc., Carteret, N.J. 07008. Diffusion of reactant through the disc was negligible because of the very small total cross-sectional area of the holes (21 holes of 0.001-in. diameter). The face opposite the working surface was insulated by drawing a solution of asphalt wax (Apiezon W black wax, James G. Biddle Co., Plymouth Meeting, Pa. 19462) in carbon tetrachloride through the disc, after cementing it to the auxiliary-electrode compartment. The auxiliary-electrode compartment was then filled with water to protect the coating, and the working surface was thoroughly cleaned.

A current-potential curve obtained with a micrometer-based porous-boundary cell is shown in Figure 12. It exhibits virtually no distortion, in contrast to the result obtained with the conventional electrode configuration. A similarly dramatic improvement is observed in the chronopotentiometric results (Figure 13), and the time required to complete a controlled-potential electrolysis is considerably decreased (Figure 14).

The porous-boundary electrode shown in Figure 17, which is particularly convenient for general use, is constructed similarly to a conventional immersible electrode (Figure 9), except that the precision-bore tube is fabricated from Corning 7930 "porous Vycor" glass, cemented rather than welded into place and surrounded by a separate auxiliary electrode compartment. A

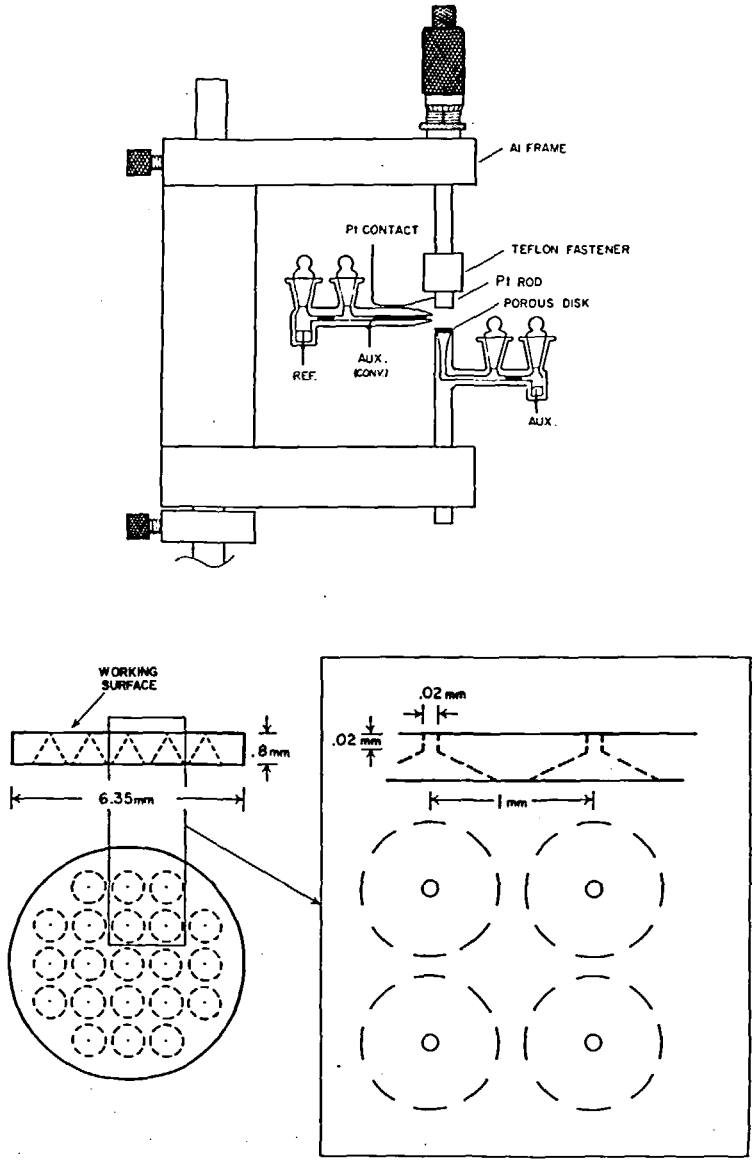

FIGURE 16. Micrometer thin-layer electrode with spinnerette porous boundary. (Reprinted from Reference 12 by courtesy of the American Chemical Society.)

process for precise annealing and shrinking of porous glass has been developed which provides the necessary precision bore, minimizes the tendency of the glass to shatter when heated, and decreases the rate of diffusion of typical electrolytes through the glass to suitable levels (Wilmad Glass Co., Buena, N.J. 08210).

Porous-boundary cells show promise of opening up a number of otherwise difficult lines of investigation, such as studies of the rates of electrode reactions in dilute or weakly ionized electrolytes, general reactivity relationships in cryogenic solutions, and the impedance characteristics of solid electrodes under a.c. polarization. The clean surfaces, simple equations, and accurate results provided by thin-layer electrodes can be exploited to study a variety of difficult solvent systems. These include organic electrode reactions, particularly in aprotic media; solutions of widely varying dielectric constants; liquefied gases; unstable electrogenerated species such as free radicals; liquid-crystal solutions; and the con-

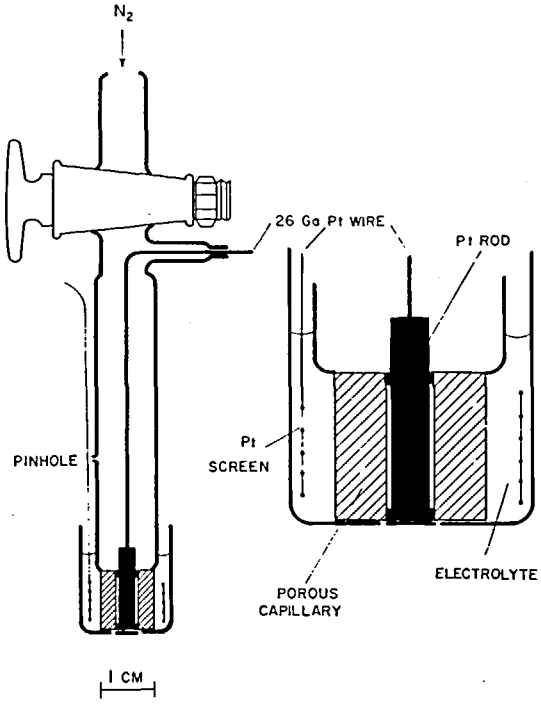

FIGURE 17. Immersible porous boundary thin-layer electrode.[37]

centrated reactant solutions encountered in studies of ionic association, solubility or phase relationships.

3. Thin-layer Electrodes for Use in Studying Electrogenerated Chromophores

Reactants confined within the thin-layer cavity are completely electrolyzed within a few seconds. It may, therefore, often be possible to electrogenerate unstable, rare, or elusive compounds for immediate spectroscopic characterization without removal from the cavity. An electrode designed for use while mounted in the sample compartment of a spectrometer[25] is shown in Figure 18. It is constructed by confining a fine gold grid (Buckbee Mears, St. Paul, Minn. 55101) between glass microscope slides, using plastic spacers to establish an average solution layer thickness, ℓ, of about 4 x 10^{-3} cm. Spent solution is removed from the cell by applying pressurized nitrogen at point A. The gold grid, B, was limited to the lower portion of the cell to minimize ohmic polarization of the solution layer. A disadvantage of this design is that the length of the light path through the solution layer is relatively short (about 10^{-4} cm), limiting its use to highly absorbing species (having molar

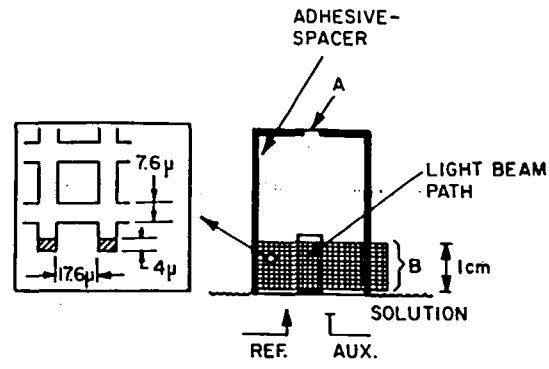

FIGURE 18. Optically transparent gold-grid thin-layer electrode. Detail at left shows grid dimensions. (Reprinted from Reference 25 by courtesy of the American Chemical Society.)

absorptivities greater than about 10^3 l mol^{-1} cm^{-1}). Cells in which the light beam is made to pass repeatedly through the layer will probably allow this difficulty to be overcome.

An optical thin-layer electrode design adapted for use with an infrared spectrometer has been described.[26]

An optical thin-layer electrode having vapor-deposited, semitransparent metal-film electrode surfaces has been described.[27] Vapor-deposited films offer the advantages, over metal grids, that greater optical and electrical uniformity is possible and a larger selection of metals is available, and the disadvantage that they occasionally display optical, electronic, or chemical characteristics different from those of massive metallic electrodes.

4. Thin-layer Electrodes for Use in Ultrahigh Vacuum

Several powerful electron, photon, and spectroscopic techniques for characterization of surfaces in ultrahigh vacuum have now been perfected to the point of general usefulness. Low-energy electron diffraction (LEED) is an invaluable indicator of the surface symmetry and, indirectly, the surface structure of metals.[38] Auger electron spectroscopy (AES), a technique having a close experimental relationship to LEED, provides semiquantitative elemental analyses of surface monolayers for potentially all of the elements except H and He,[39] particularly layers of light-atom compounds on heavy-metal surfaces. Photoelectron spectroscopy using either ultraviolet (PES) or x-ray (ESCA) excitation readily yields data from

which the position and ordering of surface electronic energy levels can be deduced.[40] Electron-stimulated desorption (ESD) with monitoring of the desorbed species by mass spectrometry[41] allows the molecular composition of adsorbed layers to be studied.

However, the successful application of electron and photon surface spectroscopic techniques to the study of electrochemically important samples requires that the electrochemical procedures be carried out without contamination either of the vacuum system or the electrode surface. An apparatus in use for this purpose in the author's laboratory[42] is illustrated in Figure 19.

An ultrahigh vacuum chamber, constructed from no. 304 stainless steel, having a large number of flanged openings suitable for installation of electronic, mechanical, optical, and vacuum accessories, provides the work space for the experiment (Model 240 chamber, Varian/Vacuum Division, Palo Alto, Calif. 94303). Pumping is accomplished by means of a fast-cycle system based upon sorption fore pumps (two), triode type ionization pumps (five), and a titanium sublimation unit (Varian, model no. FC12E). Movement of the sample crystal is achieved through a flexible steel bellows, controlled by a specially constructed external orientation device that provides precise adjustment along orthogonal X, Y, and Z axes, angular motion in the XY and XZ planes, and

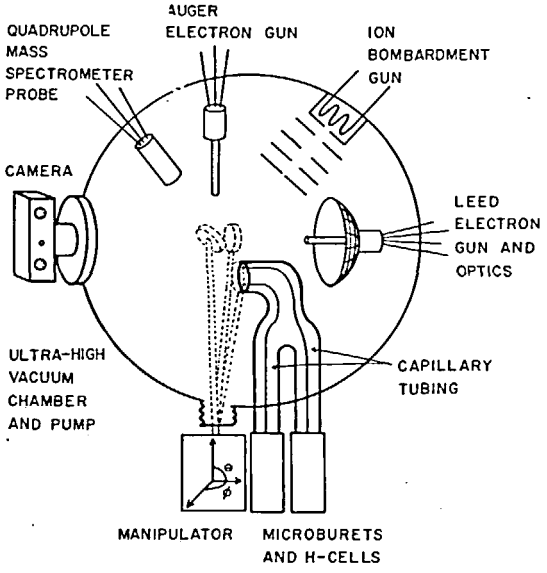

FIGURE 19. Schematic diagram of a vacuum thin-layer electrode system.[42]

180° rotation about the X axis. Final cleaning of the electrode surface is accomplished by bombardment at glancing incidence with 300 eV Ar^+ ions in the presence of 2×10^{-5} torr of pure argon. Microscopic surface disorder caused by ion bombardment is removed by resistance heating, in which a C-shaped metal foil (0.12 mm thick x 6 mm wide x 25 mm long) to which the crystal is spot welded serves as the heating element. LEED patterns are observed by means of a four-grid retarding-field energy analyzer and phosphorescent screen with integral low-energy electron gun, mounted at the rear of the chamber, opposite the viewport. The electron gun for Auger excitation of the sample is mounted at right angles to the energy analyzer and in the plane of the crystal, so that AES and LEED experiments may be performed in sequence after minor external adjustment of the position of the sample. A quadrupole mass probe is also mounted in the plane of the crystal for use in ESD experiments in which the LEED electron gun serves to stimulate desorption from selected portions of the sample. Preliminary examination of the low-energy photoelectron spectrum is possible, using a line source in the UV region and the LEED energy analyzer with a modified electronic control unit.

In preparation for electrochemical experiments following spectroscopic characterization of the electrode surface, the sample is positioned in contact with the end of the glass capillary, which is about 6 mm in diameter and recessed slightly at its center so that a thin-layer cavity about 0.02 mm deep and 5 mm wide is formed; the sample and capillary are then enclosed in a crystal-isolation valve and brought to room pressure with prepurified argon, while all other components are maintained at ultrahigh vacuum. A principal advantage of thin-layer electrodes for precise surface studies is that the volume of fluid contacting the electrode during each trial is only about 10^{-3} cm^3 per cm^2 of electrode area. Because this is very small, the probability that surface contamination will be extensive is also small. This follows from the fact that the amount of material in one monolayer (about 2×10^{-9} mol cm^{-2}) corresponds to a concentration in the cell of 2×10^{-3} *M*. Thus, surface contamination will not occur so long as the level of adsorbable impurities is kept within moderate limits.

Two separate parallel solution paths are provided by the capillary unit (Figure 19), with the

thin-layer electrode surface connected to the auxiliary electrode through one capillary and to the reference electrode through the other, so that inclusion of an ohmic potential difference in the measured electrode potential is avoided. The outer surface of the capillary unit is coated with a baked-on film of gold or platinum (Engelhard Industries, Carteret, N.J. 07008) to prevent charge from collecting on the glass surface. The microburets used to introduce electrolyte (Cole-Parmer Instrument Corp., 7425 No. Oak Park Ave., Chicago, Ill. 60648) are connected to the capillaries by means of Teflon or Kel-F fittings (Hamilton Co., Reno, Nevada) which can be removed through a valve so that only the sample and the capillary unit are present during evacuation.

After electrolysis has been completed and the electrode rinsed of nonvolatile constituents, the isolation valve is evacuated quickly to about 10^{-6} torr by an auxiliary pumping system and then opened to the main vacuum system. Characterization of the electrochemically treated sample can then be carried out by means of LEED, AES, PES, ESD/MS, and related techniques, as described above.

B. Circuitry

Almost any commercial or laboratory-built circuit capable of three-electrode potentiostatic or galvanostatic operation will suffice for thin-layer electrochemistry. Circuits constructed in the author's laboratory for use with thin-layer cells are prewired to perform linear-potential-sweep voltammetry and potential-step coulometry, and contain spare components interconnectable by means of patch cords to form the less commonly used configurations. Since thin-layer electrochemistry involves the use of small currents and long times, it is advisable to select circuit components having a high degree of stability, if necessary at the expense of current capacity and speed. The use of a single type of operational amplifier (such as Model 1009, Philbrick/Nexus Research, Dedham, Mass. 02026) throughout the circuit leads to considerable simplification without loss of performance. Currents in the range from 10 to 100 mA are supplied by booster amplifiers (Model BQ-100, Philbrick/Nexus Research). The power supply has short-circuit protection, optimal ripple (less than 1 mV RMS) and regulation characteristics (± 0.02 V), and moderate output current (± 100 mA) (Model 2203, Philbrick/Nexus Research). Shielded cable, of minimum practical length, is used for all connections to amplifier summing points. Each amplifier is connected separately to the power supply. Graphical recorders having X and Y voltage axes are used for analog data collection (Series 2000, Houston Instruments, Bellaire, Texas 77401, or Model 135, Hewlett-Packard/Neely, 3939 Lankershim Blvd., North Hollywood, Calif. 91604). The operational feedback concepts employed in design of these circuits are suitably described in various texts.[43,44]

IV. EXPERIMENTAL EXAMPLES

Various features of thin-layer cells have prompted their use for studies of the stoichiometries of complicated reactions,[3,5,9,10,13,21,22,45,46] the rates of electrode reactions,[3,6,8-10,22,47] the rates of reactions of electrogenerated reagents,[15,16,26,48-52] and the properties of molten salt solutions[33,63] and for evaluations of diffusion coefficients,[15,53,54] interfacial excesses of reactants,[3,9-11,34,50,56] and the reactivities of adsorbed molecules[9,10] and of metallic monolayers.[57-62] Applications directed toward solving practical or fundamental problems are emphasized here, although references to articles describing exploratory applications or proposed uses are given as well.

A. Stoichiometry and Composition

Thin-layer voltammetry, coulometry, and chronopotentiometry have been exploited for measurement of n values, concentrations, and formal potentials because they are governed by equations which are simpler than their conventional counterparts, do not contain diffusion coefficients, and apply to any number of repetitive cycles.[3,5,13,21,22,45,46]

An early and rather characteristic application of TLE was to the study of complexes of Pt(II) and Pt(IV).[3,5-7,9,10,22,45,47] The results of a previous study employing conventional chronopotentiometry as the measuring technique,[64] which were irreproducible and difficult to interpret owing to a critical dependence on surface state and rather complicated stoichiometry, had led to the reaction scheme

$$PtCl_6^{2-} + Pt \rightleftharpoons Pt(I) + Pt(III) \qquad (117)$$

$$Pt(I) + e^- \rightleftharpoons Pt \quad (118)$$

$$PtCl_4^{2-} + 2Cl^- \rightleftharpoons PtCl_6^{2-} + 2e^- \quad (119)$$

This gave way rather quickly to the presently accepted formulation demonstrated by means of TLE data:[45]

$$PtCl_6^{2-} + 2e^- \rightleftharpoons PtCl_4^{2-} + 2e^- \quad (120)$$

$$PtCl_4^{2-} + 2e^- \rightleftharpoons Pt + 4Cl^- \quad (121)$$

$$PtCl_4^{2-} \overset{\text{aq. HCl}}{\rightleftharpoons} x\ \underline{\text{trans}}\text{-}Pt(H_2O)_2Cl_4 + (1 - x)\ PtCl_6^{2-} + 2e^- \quad (122)$$

where x depends upon the experimental conditions. Subsequent experiments have revealed some of the mechanistic features of these ligand-bridged electrode reactions, such as the role of the double layer,[8,10,22,47] the number of electrode sites required to form the transition state,[8,10] and the influence of the electronic structure of the reactant,[6] as described in Section B below.

A useful advantage of thin-layer cells for preliminary investigations of new systems has been that n and C^0 can be determined separately from a single experiment. This is because the total charge, Q, for electrolysis of the reactant varies as n, whereas the voltammetric peak current varies as n^2 (or $*an$); for instance, combining Equations 3 and 4 for reversible reactions gives

$$n = \frac{4RT\ i_p}{F(-r)Q} \quad (123)$$

and

$$c^0 = Q/nFV \quad (124)$$

For irreversible reactions the analysis depends upon the particular form of the electrode rate law that applies, but the results are of similar usefulness to Equations 123 and 124.

The ionic charge of a reactant can be deduced, provided that the reaction is not too fast to permit the measurement of $*a$ and $*k^0$ by thin-layer methods, by inserting the values of $*a$ and $(1 - *a)$ obtained from the cathodic and anodic peak currents (Equations 21 and 22) into equations that relate the double-layer influence to the reactant charge (Part II, Section 6 above). Preliminary studies of several porphyrin derivatives have been reported in which optical thin-layer electrodes were used to obtain the n values and potentials that characterize the multistep electrode reactions of these compounds and to record the absorption spectra of the products.[46]

Studies of several well-behaved organic reactants in nonaqueous electrolytes were reported in Reference 21.

B. Kinetics

1. Rates of Electrode Reactions

Thin-layer voltammetry obeys very simple experimental equations (Part II), provides unusually clean surface conditions, and is therefore well suited to determinations of the rates of electrode reactions.

A detailed mechanism for the halide-bridged interconversion of Pt(II) and Pt(IV) complexes (Figure 20) has been formulated and tested by means of thin-layer voltammetry. Current-potential curves, such as shown in Figure 21, were recorded with all concentrations held constant except those of the platinum complexes, and apparent values of $*k^0$ and $*a$ were calculated from the peak current and potential by expressions analogous to Equations 21 to 26. Even when more than one product resulted from the electrode reactions, as in Curve C of Figure 21, the rate parameters could still be extracted directly from the current-potential curve by taking advantage of the fact that Equation 4 allows the quantity of each species to be calculated from the area of the corresponding peak. Figure 21 also illustrates the expected increase in $_ai_p$ (anodic currents are plotted upward) on passing from positively to

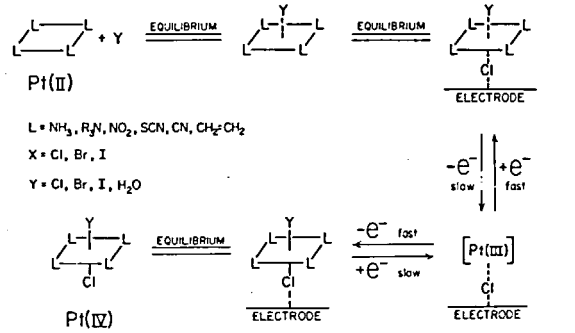

FIGURE 20. Axial ligand bridge mechanism for the Pt(IV)-Pt(II) interconversion at electrodes. (Reprinted from Reference 6 by courtesy of the American Chemical Society.)

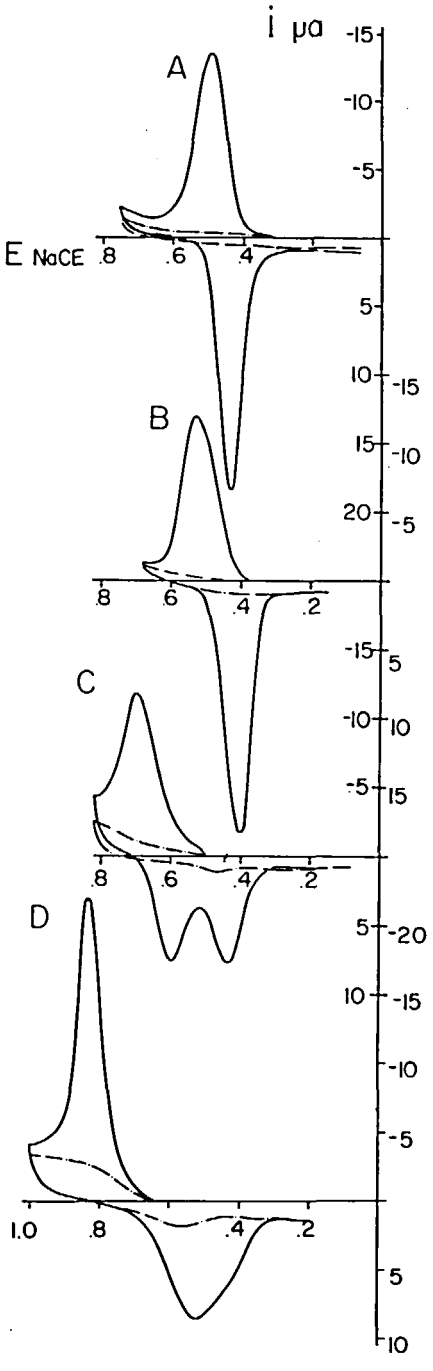

FIGURE 21. Thin-layer cyclic current-potential curves for Pt(II) and Pt(IV) complexes in chloride solutions. Curve A. $[Pt(NH_3)_4]^{2+}$; Curve B. [Pt(diethylenetriamine)NO_2]$^+$; Curve C. [*cis*-$Pt(NH_3)_2(NO_2)_2]^0$; and Curve D. $[Pt(NO_2)_4]^{2-}$. Experimental conditions: the reactant solution contained 10^{-3} *F* Pt(II), 10^{-2} *F* Cl^-, and 1 *F* $HClO_4$; A = 1.0 cm^2, $\ell = 2.65 \times 10^{-3}$ cm, $|r| = 2$ mV sec^{-1}, T = 296 ± 1°K, and V = 2.65×10^{-3} cm^3 (Curves A-C) or 3.77×10^{-3} cm^3 (Curve D). (Reprinted from Reference 22 by courtesy of Elsevier Publishing Co.)

negatively charged reactants (Curve A to D) due to electrostatic interaction of the reactant with the electric field (Part II, Section A); the cathodic current displays the opposite trend, as expected.

In order to elucidate the role of the compact layer in electrolysis of platinum complexes, the electrodes were exposed to a variety of ionizable substituted olefins, each of which reacted rapidly with the platinum surface to form a chemisorbed monolayer that was not removed by solvents or by electrolysis, except at very positive potentials. Current-potential curves obtained for platinum complexes at clean and at coated electrodes were then compared.[10] Equation 125 reflects the observed rate influence of the chemisorbed species:

$$\Delta(\text{electrode rate}) = (1-\theta)^N \exp(-ZF\Delta\Phi_2/RT) \quad (125)$$

where θ is the fractional coverage of surface by olefin, N is the number of contiguous electrode sites required to form the transition state, Z is the ionic charge of the reactant, and $\Delta\Phi_2$ is the change in potential at the outer Helmholtz plane (for the reactant) caused by the adsorbed, ionizable olefin. That is, the chemisorbed coating *accelerated* the reaction when its charge was opposite to that of the reactant, but slowed the reaction otherwise (Figure 22). The variation of Φ_2 with coverage depends on the average *position* of the ionized substituent in relation to the remainder of the double layer. Determination of the precise extent of steric hindrance due to chemisorbed surfactant as a function of coverage reveals that exactly two adjacent electrode sites are required to form the rate-limiting intermediate in the halide-bridged reduction of a platinum(IV) complex.

Accurate determination of surface coverage by adsorbed material in thin-layer cells[3,9-11,34,55,56] has been essential to these experiments (Part IV, Section B).

2. Rates of Reaction of Electrogenerated Reagents

The feasibility of determining reaction rates of reactants electrogenerated at thin-layer electrodes has been suggested[15,52] and demonstrated[16,26,48,49-51] in a number of publications. These show the approach to be particularly suitable for the study of slow reactions, requiring 10 sec or longer for appreciable change of composition, for which the performance of conventional cells is marred by convection. However, it may be worth pointing

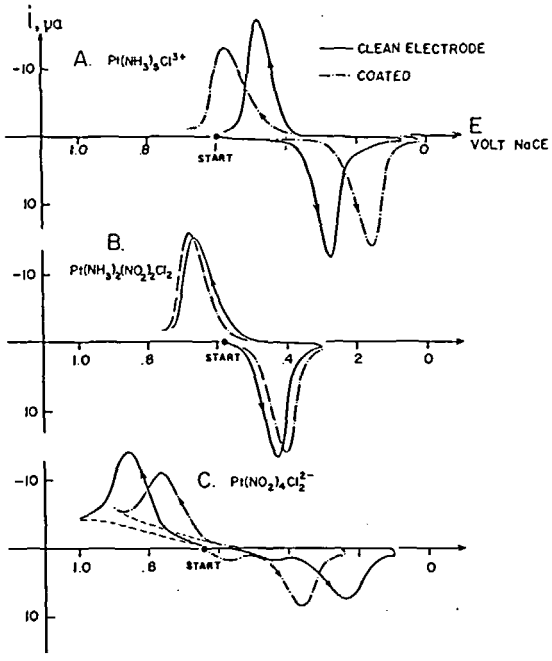

FIGURE 22. Thin-layer current-potential curves for platinum complexes at allylamine-coated platinum electrodes. (·····) Coated electrodes; (———) Clean electrodes. Experimental conditions: the reactant solution contained 10^{-3} *F* Pt(IV) (= C^0), 10^{-2} *F* NaCl, and 1 *F* $HClO_4$; A = 1.15 cm^2; Γ(allylamine) = 0.76 x 10^{-9} mol/cm^2; |r| = 2 mV sec^{-1}; T = 296 ± 1°K; and V = 3.88 x 10^{-3} cm^3. (Reprinted from Reference 9 by courtesy of the American Chemical Society.)

out that the overly complicated treatments given this approach in the literature tend to obscure its stark simplicity. The unnecessary complexity can be avoided by designing the experiment so that chemical reaction takes place to only a negligible extent during electrogeneration and subsequent electroanalysis.

For example, in the earliest application of TLE to kinetics,[48] thin-layer chronopotentiometry was employed to measure the rate at which *p*-benzoquinoneimine, electrogenerated from *p*-aminophenol, hydrolyzed in keeping with a first-order rate law to give electroinactive products (Figure 23):

$$R - ne^- \rightleftharpoons Ox \xrightarrow{k} P \qquad (126)$$

During the electrogeneration period ($O < t \leq t_f$), the rate of chemical transformation could *not* be ignored under the conditions employed. Hence,

$$\frac{dC_{Ox}}{dt} = \frac{i}{nFV} - kC_{Ox} \qquad (127)$$

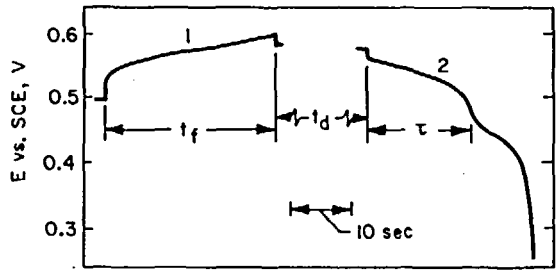

FIGURE 23. Thin-layer chronopotentiograms, with time delay and current reversal, for *p*-aminophenol. Segments 1 and 2 arise from the oxidation of *p*-aminophenol to *p*-benzoquinoneimine and the reduction of *p*-benzoquinoneimine to *p*-benzoquinone, respectively. Experimental conditions: C^0 = 1.01 x 10^{-3} *F* *p*-aminophenol in 1.017 *F* H_2SO_4; i = 10.0 microampere; T = 298°K; t_d = 45.4 sec; and V = 2.39 x 10^{-4} cm^3. (Reprinted from Reference 48 by courtesy of the American Chemical Society.)

and accordingly, for $O < t \leq t_f$

$$C_{Ox} = \frac{i}{nFVk}[1 - \exp(-kt)] \qquad (128)$$

while during the delay period ($t_f < t \leq t_f + t_d$)

$$\frac{dC_{Ox}}{dt} = -kC_{Ox} \qquad (129)$$

which, after integration and combination with Equation 128, gives

$$C_{Ox} = \frac{i}{nFVk}[1 - \exp(-kt_f)]\exp[-k(t - t_f)] \qquad (130)$$

However, during the determination period ($t_f + t_d < t \leq t_f + t_d + \tau$), chemical change again cannot be ignored, so that

$$\frac{dC_{Ox}}{dt} = -\frac{1}{nFV} - kC_{Ox} \qquad (131)$$

which on integration gives

$$C_{Ox} = \frac{i}{nFVk}\left\{\exp[-k(t-t_f-t_d)][1 + \exp(-kt_d) \times (1 - \exp(-kt_f))] - 1\right\} \qquad (132)$$

and finally, noting that $C_{Ox} = 0$ at the transition time, τ, for the reduction of all the remaining Ox in the cavity, the desired expression is obtained:

$$\exp(-kt_d)[1 - \exp(-kt_f)] - \exp(k\tau) + 1 = 0 \qquad (133)$$

Iterative solution of Equation 133 is required to obtain the value of k from the experimental parameters t_d, t_f, and τ. Solution of the equations

for more elaborate rate laws is generally tedious. Voltammetric rate studies require equations which are even more cumbersome.[52]

As an initial simplification, the constant current is adjusted so as to make the durations of the periods of electrogeneration (t_f) and electroanalysis (τ) much shorter than that of the delay period (t_d). Under these circumstances, Equation 133 may be simplified to

$$k = \frac{1}{t_d} \ln \frac{t_f}{\tau} \qquad (134)$$

That is, the thin-layer cell is simply used to effect a rapid constant-current coulometric analysis of the reaction mixture at some appropriate elapsed time following introduction of the reactant.

Since potential-step coulometry is the fastest of the d.c. thin-layer techniques and provides the greatest accuracy in correcting for background reactions, it is the logical choice for reaction-rate measurements. Thin-layer coulometric data for the above first-order reaction are related to the rate constant by Equation 135

$$k = \frac{1}{t_d} \ln (Q_f/Q) \qquad (135)$$

where Q_f is the quantity of Ox generated and Q is the quantity of Ox found after a time, t_d. This governing equation is obtained simply by inserting the measured quantities, Q_f and Q, directly into the integrated rate law. The upper limit to the range over which rate constants can be measured by thin-layer potential-step coulometry is imposed by the requirement that the half-life of the reactant, 0.693/k, be large in comparison with the time required for electrogeneration and determination. Applying Equation 50, which describes the time required to complete a diffusion-limited electrolysis in a thin-layer cell, to the present situation gives

$$k \leq \frac{0.693\ \pi^2\ D\epsilon}{\ell^2\ |\ln \epsilon|} \qquad (136)$$

For example, if $D = 10^{-5}$ cm^2 sec^{-1}, $\epsilon = 0.01$, and $\ell = 10^{-3}$ cm, then the rate can be measured within a relative error of ± 1% so long as $k \leq 0.3$ sec^{-1}. Ohmic polarization effects, which are serious at high currents, may occasionally set more stringent requirements on this and other TLE approaches, unless porous-boundary electrodes are used (Part III, Section A-2).

Numerous electroanalytical procedures for rate measurement based upon TLE and conventional electrodes have been tested by applying them to the disproportionation of electrogenerated U(V):[50,65,66]

$$U(VI) + e^- \rightleftharpoons U(V) \xrightarrow{k} \tfrac{1}{2}\,U(V) + \tfrac{1}{2}\,U(IV) \qquad (137)$$

Values of k obtained by various methods (about 105 l^3 mol^{-3} sec^{-1}) are in fair agreement. The rate law is

$$\frac{dC_{U(V)}}{dt} = -\,k(C_{H^+})\ C^2_{U(V)} \qquad (138)$$

Integration of Equation 138 at constant C_H^+ gives

$$k = \frac{1}{(C_{H^+})t}\left[\frac{1}{C_{U(V)}} - \frac{1}{C^0_{U(V)}}\right] \qquad (139)$$

The rate constant, k, is obtained in terms of the results of double-potential-step coulometry in TLE by replacing $C^0_{U(V)}$ and $C_{U(V)}$ with the quantities coulometrically generated and found after a time t_d:

$$k = \frac{FV}{(C_{H^+})t_d}\left[\frac{1}{Q(\text{remaining})} - \frac{1}{Q(\text{generated})}\right] \qquad (140)$$

Steady-state amperometry with TLE has been advocated for rate measurements,[15,16,50,51] in which the steady-state current provides a continuous record of the reactant concentration as a function of time. However, comparison of the homogeneous and electrode reaction rates for typical values of the experimental parameters indicates that irreversible side reactions must be rigorously absent if meaningful results are to be obtained. For a first-order chemical reaction

$$\frac{\text{Electrode reaction rate}}{\text{Chemical reaction rate}} = \frac{i_L/nF}{kCV} \qquad (141)$$

where i_L is given by Equation 92. Thus, if $D_{Ox} = D_R = 10^{-5}$ cm^2 sec^{-1}, $k = 10^{-2}$ sec^{-1}, and $\ell = 10^{-3}$ cm, then

$$\frac{\text{Electrode reaction rate}}{\text{Chemical reaction rate}} = \frac{2D}{k\ell^2} = 2000 \qquad (142)$$

Each reactant molecule undergoes electrochemical oxidation *and* reduction an average of 2000 times before succumbing to the chemical reaction.

3. Diffusion Coefficients

Two-electrode steady-state amperometry[15] can be employed to measure diffusion coefficients,

D_{Ox} or D_R, when the reactant concentration is such that $C_R D_R$ or $C_{Ox} D_{Ox}$ predominates, respectively (see Equations 109 and 110). This approach appears to offer the advantage that i_L depends on the first power of D rather than on $D^{1/2}$, as it does for commonly used conventional electrodes, promising more precise results, although calibration of the TLE with a reactant couple for which at least one diffusion coefficient is accurately known would generally be required.

Two-electrode amperometry has been used for studies of diffusion and migration of species in iodide-iodine solutions,[54] yielding values of diffusion coefficient that are in reasonable agreement with those obtained by other methods, and indicating that the effects of electrical migration can be neglected even in the absence of supporting electrolyte if ΔE less than 50 mV and that convection is minimal if ℓ is less than 0.2 mm.

C. Adsorbed Molecules

1. Measurement of Interfacial Excess

The earliest application of TLE to the study of reactant adsorption[3,34,55,56] resolved a series of apparent conflicts[67] in the literature concerning chemisorption of iodide and iodine on platinum surfaces.[67-72] Radiotracer studies[67] had clearly indicated that I^- and I_2 form species so strongly adsorbed onto platinum that they cannot be rinsed from the surface at open circuit, whereas conventional electrochemical methods did not reveal the presence of adsorbed I^- and seemed to indicate that adsorbed I_2 was readily rinsed from the surface.[70,71] Meanwhile, adsorbed species containing iodine species were postulated as intermediates in certain electrochemical reactions.[67,69,72]

When a TLE was rinsed and filled with a dilute solution of I_2 in 1 *F* H_2SO_4, the total charge consumed upon reduction of all of the I_2 in the cell to I^- exceeded that for the I_2 contained in the solution layer by an amount which corresponded to approximately monolayer coverage:[55]

$$Q - Q_b = 2FVC^0_{I_2} + 2FA\,\Gamma_I \text{ (reducible)} \qquad (143)$$

This reducible, adsorbed iodine could be readily rinsed away, in keeping with earlier observations;[70] however, TLE current-potential curves obtained after rinsing with I_2 solution followed by pure supporting electrolyte exhibited anodic and cathodic peaks corresponding to oxidation of adsorbed I_2 to IO_3^- (E_p = 1.0 V vs. N.C.E.) and reduction of IO_3^- to I_2 (E_p = 0.8 V);[34] the adsorbed amount followed Equation 144:

$$Q - Q_b = 5FA\,\Gamma_I \text{ (non-reducible)} \qquad (144)$$

Thus, part of the earlier conflict[67] is resolved by noting that I_2 is adsorbed in two forms, one of which is not reducible.

When a TLE was rinsed and filled with I^- solution, the charge consumed upon oxidation of I^- to I_2 (at potentials near the standard potential of the I_2/I^- couple) was merely that due to dissolved I^-:

$$Q - Q_b = FVC^0 \qquad (145)$$

However, current-potential curves for electrodes rinsed with I^- and then with pure electrolyte indicated the presence of an adsorbed species oxidizable to IO_3^-. Confirmation of the presence of difficultly reactive adsorbed I^- was obtained from experiments in which I^- solution was added to the cleaned surfaces of a micrometer thin-layer cell by means of a microburet;[55] the charge required for oxidation of dissolved I^- to I_2 corresponded to Equation 146, thus confirming the relative unreactivity

$$Q - Q_b = \begin{cases} 0, \text{ if } FVC^0_{I^-} \le FA\,\Gamma_{I^-} \\ FVC^0_{I^-} - FA\,\Gamma_{I^-}, \text{ otherwise} \end{cases} \qquad (146)$$

of the adsorbed species formed when Pt is rinsed with I^- solution.

Coulometric determination of IO_3^- produced in the TLE cavity by oxidation of adsorbed I^- has been exploited to determine the extent of surface coverage by olefins.[10] It is found that if the electrode is first exposed to the olefin and then rinsed with I^- solution, an amount of I^- is adsorbed that corresponds to the electrode area remaining uncovered by olefin. That is, the iodide served to "titrate" unoccupied surface area without displacing previously adsorbed olefin.

2. Reactivity of Adsorbed Molecules

Thin-layer voltammetry and coulometry have yielded precise and definitive data regarding the stoichiometries, rates of reduction, and stabilities of organic depolarizers and metal complexes connected to Pt surfaces through olefinic carbon chains.[9]

Figure 24 shows current-potential curves for four typical substituted olefins chemisorbed at Pt surfaces in 1 F $HClO_4$. In this figure, i_r and i_c denote the currents observed for reactant-coated and clean surfaces, respectively, and i_b represents the background current due to oxidation of the uncoated portion of the electrode surface; $i_r(corr.)$ is given by

$$i_r(corr) \equiv \begin{cases} i_r - i_b, & \text{for } E \leq E_{ch} \\ i_r - i_c, & \text{for } E > E_{ch} \end{cases} \qquad (147)$$

where E_{ch} is defined by the figure. Substitution of i_c for i_b in Equation 147 when $E \gg E_{ch}$ reflects the fact that massive oxygen electrogeneration rather than surface oxidation becomes the predominant background reaction at very positive potentials. The curves labeled i_{th} are graphs of Equation 148, which is derived in Reference 9.

$$i_{th} = e\, a i_p \exp\left\{\frac{-(e)\, a i_p}{nFAr\, \Gamma_R^0}(E - a E_p) - \exp\left[\frac{-(e)\, a i_p}{nFAr\, \Gamma_R^0}(E - a E_p)\right]\right\} \qquad (148)$$

Since the reactive entity in each case is the Pt-C linkage derived from the electrode and the double bond, very similar current-potential behavior is expected and observed. The predominant oxidation path is

$$H_2{}^*C = CH\text{-}R\text{-}X_{(ads)} + 4H_2O \xrightarrow{1\ F\ HClO_4} {}^*CO_2 + HOOC\text{-}R\text{-}X + 10\ H^+ + 10\ e^- \qquad (149)$$

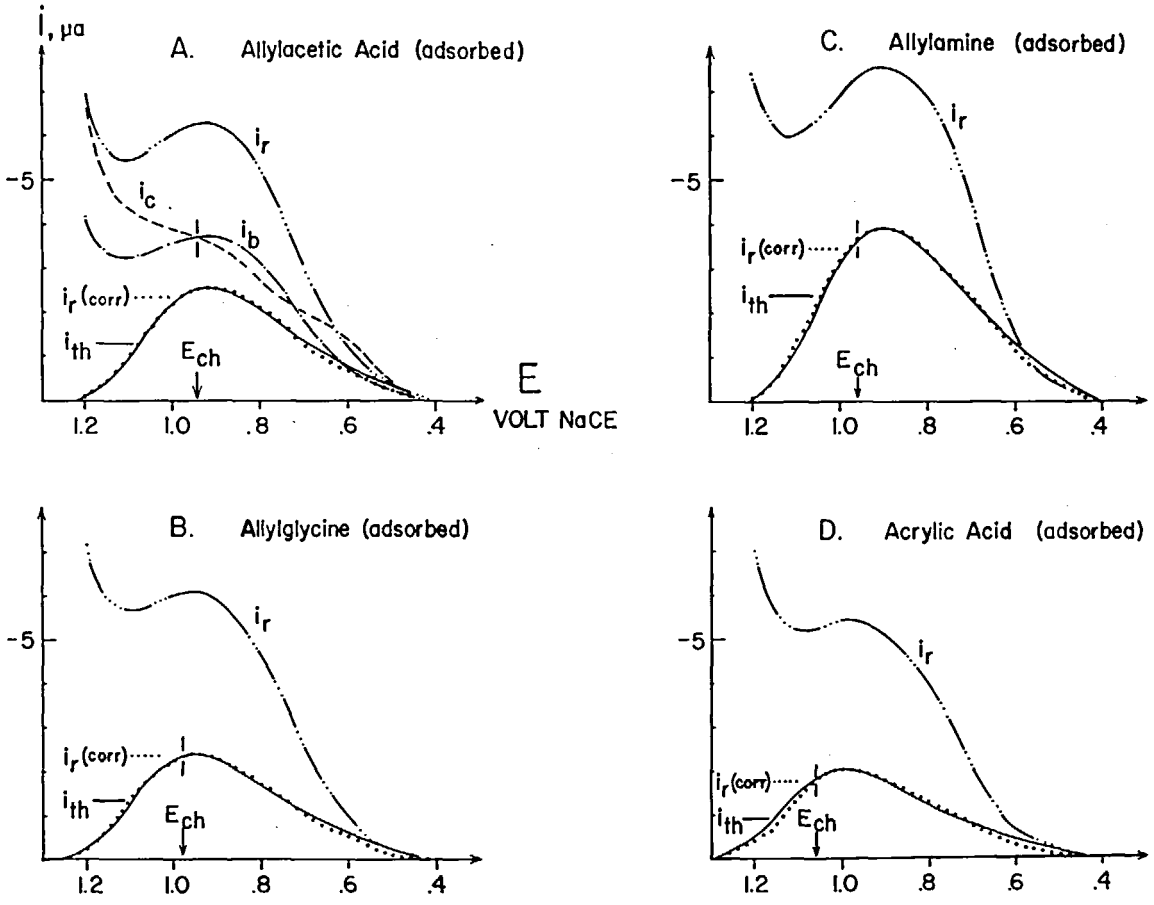

FIGURE 24. Thin-layer current-potential curves for oxidation of olefins chemisorbed at Pt electrodes. (See text for definitions of i_r, i_c, i_b, i_{th}, $i_r(corr)$, and E_{ch}.) Experimental conditions: the supporting electrolyte was 1 F $HClO_4$; A = 1.15 cm^2; r = 2 mV sec^{-1}; T = 296 ± 1°K; and V = 3.88 x 10^{-3} cm^3. For allylacetic acid, $\Gamma_R{}^0$ = 0.49; for allylglycine, 0.46; for allylamine, 0.76; and for acrylic acid, 0.43. (Reprinted from Reference 9 by courtesy of the American Chemical Society.)

where H_2*C=CH–R–X is acrylic acid, allylacetic acid, allylamine, 4-allylcatechol, 4-allyl-2,6-dimethoxyphenol, allylglycine, 2-allylhydroquinone, 4-allyl-2-methoxyphenol, 6-allyl-2-methoxyphenol, allyltriethylammonium perchlorate, fumaric acid, or vinylsulfonic acid.

The electrochemical reactivities of 2-allylhydroquinone and other diphenol derivatives having allyl side chains have been studied.[9] These compounds are rapidly chemisorbed from their dilute aqueous solutions, presumably by attachment at the allylic double bond. Surprisingly, the chemisorbed forms of these compounds are unreactive, although the dissolved species show the rapid reversible electrode behavior characteristic of quinone-hydroquinone couples (Figure 25). Examination of molecular models suggests a possible explanation: adsorption of the allylic double bond onto the platinum surface places the methylene group, and particularly the methylenic protons, rather close to the surface. In the most stable conformer, the aromatic ring is normal to the surface and on the opposite side of the adsorbed chain, and the distance of the aromatic ring from the surface and/or its vertical orientation may then prevent it from reacting. In view of this explanation, diphenols having five or more carbons between the aromatic ring and the adsorbing double bond would be expected to be reactive when chemisorbed; chemisorbed 2-(1-hydroxyhept-6-enyl) hydroquinone was found to be electrolyzed reversibly at potentials close to the standard potential for dissolved material, lending support to the above explanation.

Coordination compounds connected to the electrode surface through chemisorbed olefinic ligands have been prepared.[9] For example, a platinum surface rinsed with a solution of allylamine and soaked in a solution of Pt(IV) or Pt(II) soon acquires a monolayer of chemisorbed allylamine complexes. Since the resulting complexes are nonlabile, they are not removed from the surface by rinsing, and their electrochemical properties can, therefore, be studied in the absence of dissolved reactants. The reactivities of these "two-dimensional" platinum complexes resemble those of their unadsorbed counterparts, although the influence of surface orientation is apparent.

A particularly suggestive example of two-dimensional coordination chemistry is provided by allylsalicylic-acid-coated Pt TLE in solutions containing Fe(II). The coated electrode acquires a

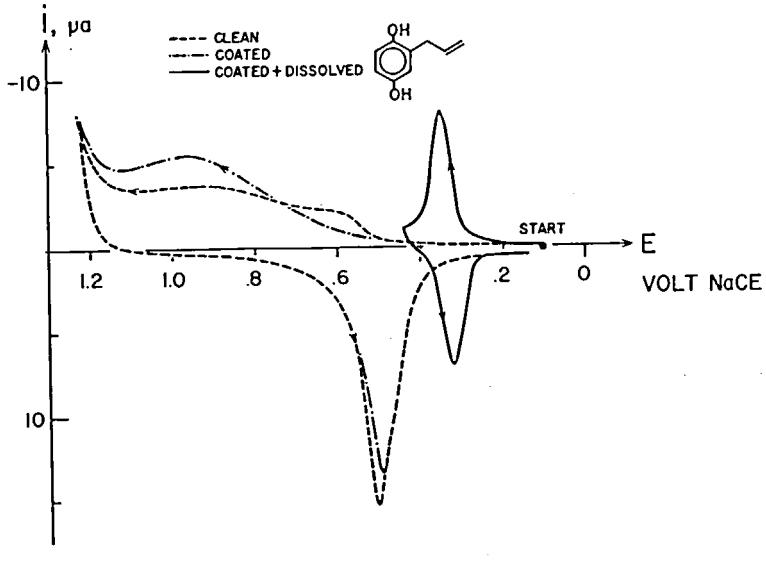

FIGURE 25. Thin-layer current-potential curves for 2-allylhydroquinone at platinum electrodes. (----) clean electrode; (·····) chemisorbed 2-allylhydroquinone; and (————) 2-allylhydroquinone chemisorbed and also present in the solution. Experimental conditions: the supporting electrolyte was 1 *F* $HClO_4$; A = 1.15 cm^2; $C^0 = 2 \times 10^{-3}$ *F*; $|r| = 2$ mV sec^{-1}; T = 296 ± 1°K; and V = 3.88 x 10^{-3} cm^3. (Reprinted from Reference 9 by courtesy of the American Chemical Society.)

monolayer of Fe(II) when rinsed with dilute Fe(II) solution at potentials corresponding to zero electrode electronic charge, due to chelation with the chemisorbed allylsalicylate. At more positive potentials, however, an interfacial excess does not develop, presumably because the positively charged electrode attracts the salicylate dianions away from Fe^{2+} ions in the diffuse layer while repelling the Fe^{2+} ions. Determinations by thin-layer coulometry of the interfacial excess of Fe(II) as a function of electrode potential yielded the results shown in Figure 26, from which it can be seen that the chelate-coated electrode performs as a "tunable" ion-exchange resin, whose partition coefficient can be controlled by means of the electrode potential. The solid curves shown in Figure 26 are graphs of Equation 150, derived in Reference 9:

$$[1 - f(E)] \exp\left[-\frac{ZF}{RT}\frac{C}{C_d}E\right] = \frac{\exp\left[-\frac{ZF}{RT}\frac{C}{C_d}E_z\right]}{{}_zK_f\, C_{Fe^{z+}}}\frac{\rho}{1-\rho} \qquad (150)$$

where

$$f(E) \equiv \frac{1 - \exp[-\lambda(1-x_1/x_2)]}{\exp[-\lambda(1-L/x_2)] - \exp[-\lambda(1-x_1/x_2)]}$$

$$\lambda \equiv Z_s F(E-E_z)/RT$$

$$\rho \equiv \frac{\Gamma^T\,(Fe^{z+}\text{-}Sal^{2-})}{\Gamma^0(Sal^{2-})}$$

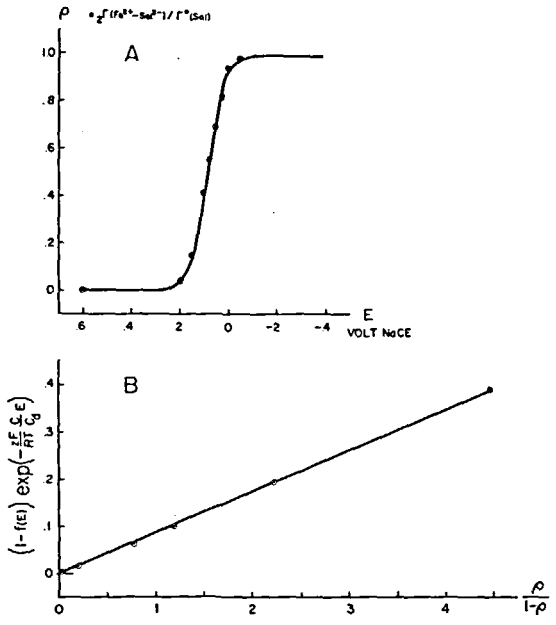

FIGURE 26. Dependence on potential of the adsorption of Fe(II) induced by chemisorbed 3-allylsalicylic acid. A. Effect of potential on the ratio of complexed to free ligand adsorbed. B. Graph for obtaining the magnitude of the stability constant at zero-field. oooo Circles denote experimental points, and solid curves are graphs of Equation 150. Experimental conditions and parameters: A = 1.15 cm^2; $C^0_{Fe(II)}$ = 1.15 x 10^{-4} *F*; C/C_d = 0.050; $\Gamma^0_{(Sal^{2-})}$ = 1.19 x 10^{-9} mol cm^{-2}; L = 7.3 Å; T = 298°K; V = 3.88 x 10^{-3} cm^3; x_1 = 2.15 Å; Z = 2; and Z_s = -2. (Reprinted from Reference 9 by courtesy of the American Chemical Society.)

$_zK_f \equiv$ stability constant for $E=E_z$,

$L \equiv$ distance of chelate from surface with chain fully extended,

$x_1 \equiv$ distance of closest approach of chelate,

$x_2 \equiv$ distance of closest approach of Fe in diffuse layer,

$Z_s \equiv$ ionic charge of surfactant-chelate, and other symbols are as defined in Part II, Section F.

D. Metal Deposition

Schmidt and co-workers have reported a series of intriguing thin-layer studies of metal deposition, in which the metal deposited was different from the electrode metal.[20,23,58-62] Metal-ion-substrate combinations were chosen for which diffusion of the deposited metal into the substrate was unlikely at room temperature (Pb^{2+}/Au; Pb^{2+}/Pt; Tl^+/Ag; Bi^{3+}/Ag). Reactant concentrations and cavity thicknesses were made small to accentuate effects accompanying deposition of the first few atomic layers on the foreign substrate.

Current-potential curves for Pb^{2+} at a clean Ag thin-layer electrode are shown in Figure 27, from which it can be seen that the reduction of Pb^{2+} gives rise to two peaks. Although structural characterization of the Pb deposit awaits the use of LEED in combination with single-crystal TLE (Part III, Section A-4), it seems clear that the first, relatively constant peak corresponds to deposition of Pb at less-than-unit surface activity, and the second to reduction at close-to-unit surface activity.

Two completely analogous anodic peaks are obtained upon reversal of the direction of potential scan (Figure 27, Curve B), confirming that the splitting stems from thermodynamic rather than kinetic causes. The potentials of the cathodic and analogous anodic first peaks (-0.425

and -0.410 V vs. SCE) are more *positive* than the rest potential for the same solution at a pure Pb electrode (-0.525 V vs. SCE). Similar behavior was obtained for a variety of supporting electrolytes, although differences in peak potentials were noted,[60] and for other ion-substrate pairs[62] or mixtures of metal ions.[61] Experiments in which the initial quantity of metal ions was gradually increased without changing the composition of the initial solution (by adjusting the thickness of the solution layer) show that the first cathodic peak reaches a constant size, while the second peak continues to increase, as is expected if the first peak corresponds to saturation of the clean Ag surface with Pb (Figure 28).

Graphical integrations of curves such as those of Figure 28 reveal that the maximum area of the first peak (and presumably the quantity of Pb required to produce a unit-activity deposit on an Ag electrode) corresponds to about 5×10^{-9} mol cm^{-2} of Pb. This coverage can be compared to the amount of iodine required to saturate a Pt surface, about 3×10^{-9} mol cm^{-2}.[34]

Schmidt and co-workers have presented equations describing the thin-layer current-potential curves observed for the metal-ion-substrate combinations that they studied.[20,61] Derivation of the equations here will employ the somewhat simpler approach presented in Part II, Section A-2. The current at the thin-layer electrode will be given by the time derivative of Faraday's law.

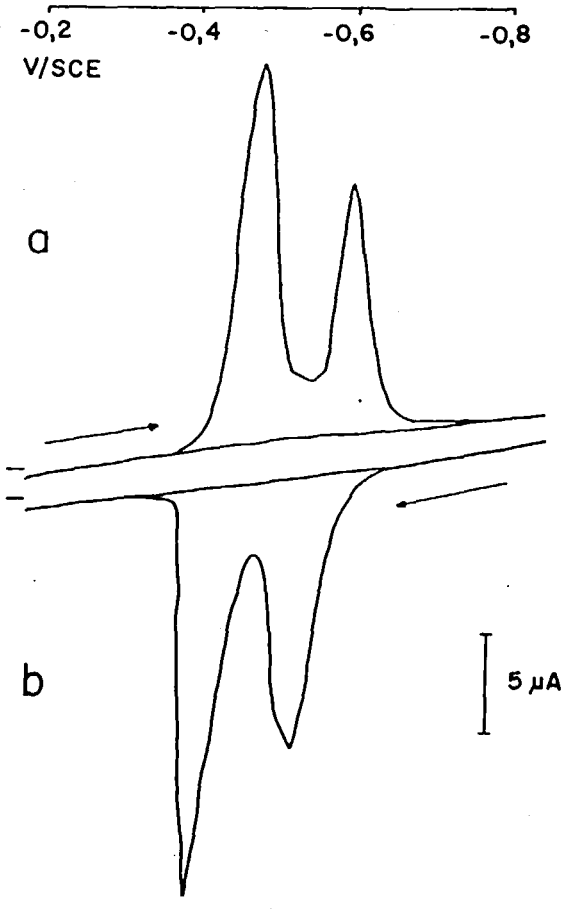

FIGURE 27. Current-potential curves for Pb^{2+} at an Ag electrode of the "chamber" micrometer design. Curve A. Reduction of Pb^{2+}. Curve B. Re-oxidation of Pb deposit. Experimental conditions: 2.61×10^{-4} *F* $PbCl_2$ and 0.5 *F* KCl; A = 0.785 cm^2; $\ell = 10^{-2}$ cm; $|r| = 3.33$ mV sec^{-1}; T = 298 ± 0.1°C. (Reprinted from Reference 20 by courtesy of the Swiss Chemical Society, Basel.)

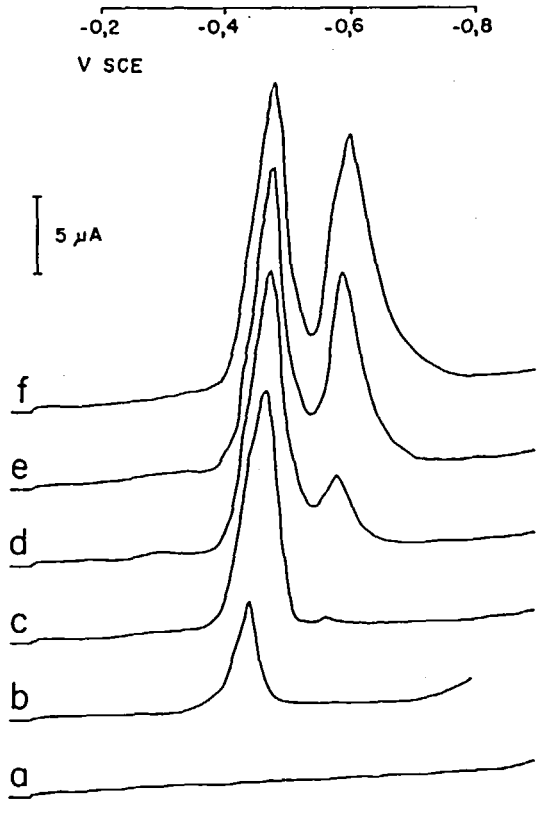

FIGURE 28. Current-potential curves for Pb^{2+} at an Ag thin-layer electrode for various solution layer volumes. Curve A. Supporting electrolyte; Curve B. $\ell = 0.000$ cm; Curve C. $\ell = 4 \times 10^{-3}$ cm; Curve D. $\ell = 8 \times 10^{-3}$ cm; Curve E. $\ell = 12 \times 10^{-3}$ cm; and Curve F. $\ell = 16 \times 10^{-3}$ cm. Experimental conditions: 2.43×10^{-4} *F* $PbCl_2$ and 0.5 *F* KCl; A = 0.785 cm^2; r = -3.33 mV sec^{-1}; and T = 298 ± 0.1°C. (Reprinted from Reference 20 by courtesy of the Swiss Chemical Society, Basel.)

$$i = -nFV\frac{dC_{Me^{n+}}}{dt} = -nFVr\frac{dC_{Me^{n+}}}{dE} = nFAr\frac{d\Gamma_{Me}}{dE} \quad (151)$$

Since the reaction studied appears to be electrochemically reversible

$$E = E^0 + \frac{RT}{nF}\ln\frac{C_{Me^{n+}}}{a_{Me}} \quad (152)$$

The relationship between surface activity, a_{Me}, and interfacial excess, Γ_{Me}, was assumed in the original publication[6] to be

$$a_{Me} = \begin{cases} K\Gamma_{Me}/({}_s\Gamma_{Me} - \Gamma_{Me}), & \Gamma_{Me} < {}_s\Gamma_{Me} \\ 1, & \Gamma_{Me} \geq {}_s\Gamma_{Me} \end{cases} \quad (153)$$

However, since this leads to a discontinuity[1] in i at $\Gamma_{Me} = {}_s\Gamma_{Me}$ and thus does not adequately represent the results, Equation 154 will be employed instead.

$$a_{Me} = \begin{cases} K\Gamma_{Me}/({}_s\Gamma_{Me} - \Gamma_{Me}), & \Gamma_{Me} < {}_s\Gamma_{Me} \\ A(\Gamma_{Me} - {}_s\Gamma_{Me})/V, & \Gamma_{Me} \geq {}_s\Gamma_{Me} \end{cases} \quad (154)$$

Here ${}_s\Gamma_{Me}$ is the saturation value (the interfacial excess developed during the first peak) and K is a constant. Since the quantity of reactant in the solution layer is constant,

$$C_{Me^{n+}} = C^0 - A\Gamma_{Me}/V \quad (155)$$

Combining Equations 154 to 156 gives

$$E = E^0 + \frac{RT}{nF}\ln\frac{C^0 - A\Gamma_{Me}/V}{K\Gamma_{Me}/({}_s\Gamma_{Me} - \Gamma_{Me})}, \quad \text{if } \Gamma_{Me} < {}_s\Gamma_{Me} \quad (157)$$

$$E = E^0 + \frac{RT}{nF}\ln\frac{VC^0/A - \Gamma_{Me}}{(\Gamma_{Me} - {}_s\Gamma_{Me})}, \quad \text{if } \Gamma_{Me} \geq {}_s\Gamma_{Me} \quad (158)$$

Equations 152, 157, and 158 together describe the current-potential curve. The theoretical current-potential curves are graphed in Figure 29. The first and second peak potentials, ${}_1E_p$ and ${}_2E_p$, are given by Equations 159 and 160, respectively,

$${}_1E_p = E^0 + \frac{RT}{nF}\ln\frac{C^0 - A\,{}_s\Gamma_{Me}/2V}{K} \quad (159)$$

$${}_2E_p = E^0 \quad (160)$$

and the peak currents are given by Equations 161 and 162

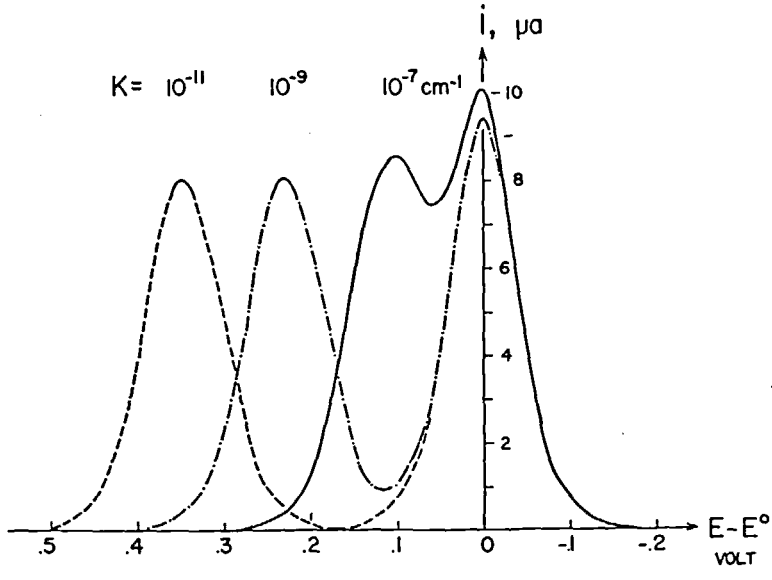

FIGURE 29. Theoretical thin-layer current-potential curves for deposition of metal on a dissimilar substrate. Graphs of Equations 152, 157, and 158. Values of the parameters assumed in making the graphs: A = 1 cm²; $C^0 = 10^{-2}$ *F*; ${}_s\Gamma_{Me} = 5 \times 10^{-9}$ mol cm^{-2}; n = 1; r = -2×10^{-3} V sec^{-1}; T = 298°K; and V = 10^{-3} cm³.

$$ {}_1i_p = \frac{n^2F^2(-r)A\ {}_s\Gamma_{Me}}{4RT} \frac{(C^0 - A\ {}_s\Gamma_{Me}/2V)}{(C^0 - A\ {}_s\Gamma_{Me}/4V)} \quad (161) $$

$$ {}_2i_p = \frac{n^2F^2(-r)V(C^0 - A\ {}_s\Gamma_{Me}/V)}{4RT} \quad (162) $$

from which it can be seen that the potential of the first peak, ${}_1E_p$, reflects the adsorption strength, K, and that the current is proportional to the saturation interfacial excess, ${}_s\Gamma_{Me}$.

The peak potentials observed for the Pb^{2+}/Ag metal ion-substrate pair in various supporting electrolytes are summarized in Table 2. The difference, ${}_1E_p - E_{rest}$, where E_{rest} is defined by

$$ E_{rest} = E^0 + \frac{RT}{nF} \ln (C^0 - A\ {}_s\Gamma_{Me}/2V) \quad (163) $$

reflects the magnitude of the quantity 1/K and thus measures the extent to which Pb prefers to deposit on the partially coated Ag substrate rather than on a pure Pb surface:

$$ {}_1E_p - E_{rest} = \frac{RT}{nF} \ln \frac{1}{K} \quad (164) $$

From Table 2 it can be seen that ${}_1E_p - E_{rest}$ varies with the nature of the supporting electrolyte anion in the order $F^- \geqslant ClO_4^- > NH_2SO_3^- > Cl^- \geqslant Br^- > SCN^- > I^-$. That is, the adsorption strength of Pb on Ag varies inversely with the strength of adsorption of the supporting electrolyte anion on Ag and other d^{10} metals such as Hg:[7] $I^- > SCN^- \geqslant Br^- > Cl^- > NH_2SO_3^- \geqslant ClO_4^- > F^-$. Therefore, it appears that the depositing metal suffers competition from adsorbed anions for sites on the Ag substrate.

E. Electrogenerated Chromophores

Visible absorption spectroscopy has been employed effectively with TLE to explore the reactivity of biologically significant porphyrin systems by Peychal-Heiling and Wilson.[46] The feasibility of such experiments was predicted[17] and confirmed[18,25,27] earlier. Spectrometers and spectral ranges offering sufficient sensitivity for use with the low concentrations (10^{-3} *F*) and short path lengths (10^{-3} cm) provided by thin-layer cells, such as visible[27] or UV-induced fluorescence, attenuated reflectance, multiple specular reflection, infrared absorption,[25] electron-spin resonance, and low-energy electron/photon techniques (Part III, Section A-4), merit special consideration in designing future experiments.

F. Molten Salts

Current-potential curves for the Cr(III)-Cr(II) couple in a LiCl-KCl eutectic melt appear in Figure 30. They show that this couple obeys the thin-layer current-potential expression for reversible reactions, Equation 2. The breadth of the peak varies as RT/nF and accordingly increases with T; i_p decreases proportionately. At the same

TABLE 2

Peak Potentials of First and Second Waves for Pb^{2+} at an Ag TLE

Supporting electrolyte	pH	$C^0_{Pb^{2+}}$ F x 10^4	${}_1E_p - E_{rest}$ (first peak) Deposition	Dissolution	${}_2E_p - E_{rest}$ (second peak) Deposition	Dissolution
0.5 *F* NH_4ClO_4	4.5	2.45	150	175	−30	0
0.3 *F* NaF	1.0	2.45	135	175	−30	10
0.5 *F* NH_2SO_3H	0.5	2.55	115	125	−35	−5
0.5 *F* KCl	4.5	2.55	100	115	−40	−5
0.5 *F* KBr	4.5	2.55	50	80	−30	10
0.5 *F* KSCN	4.0	2.55	40	75	−30	5
2.0 *F* KI	5.0	2.55	30	30	−25	−10

Experimental conditions: A = 0.785 cm^2, $\ell = 10^{-2}$ cm, $|r| = 1.67$ mV sec^{-1}, and T = 298 ± 1°K.
(Reprinted from Reference 60 by courtesy of the Swiss Chemical Society, Basel.)

time E_p becomes more negative, while dissolution of the electrode in the melt according to Equation 165

$$Pt + 4Cl^- \rightleftharpoons PtCl_4^{2-} + 2e^- \quad (165)$$

increases, so that interference between electrode dissolution and the Cr(III)-CR(II) reaction becomes appreciable at higher temperatures. Allowance was made for the decrease in cell volume and melt density and the temperature dependence of the standard potential in plotting Equation 2 for comparison with the experimental curves.

Figure 31 shows a TLE coulometric charge-time curve for Cr(III)-Cr(II) in the LiCl-KCl eutectic melt. Edge-diffusion and excessive ohmic polarization are absent. Thin-layer coulometric data obtained at several temperatures are presented in Table 1 (Part III, Section A-1).

TLE current-reversal chronopotentiograms for the Cr(III)-Cr(II) couple in the LiCl-KCl eutectic melt have the expected forms, as in Figure 32.

Voltammetric peaks involving reactions of the electrode with a pure melt are being identified and characterized in preparation for studies of electrode kinetics in nitrate melts. Although the pure $NaNO_3$-KNO_3 eutectic melt does not attack the platinum surface at open circuit, a number of common melt contaminants do so. It appears that nitrate melts involve four oxidation states of nitrogen (V, IV, III, and II) and four oxygen species (O_2, O_2^-, O_2^{2-}, O^{2-}) in addition to electrode surface oxides,[33,73,74] providing an appropriate challenge to the thin-layer method.[33]

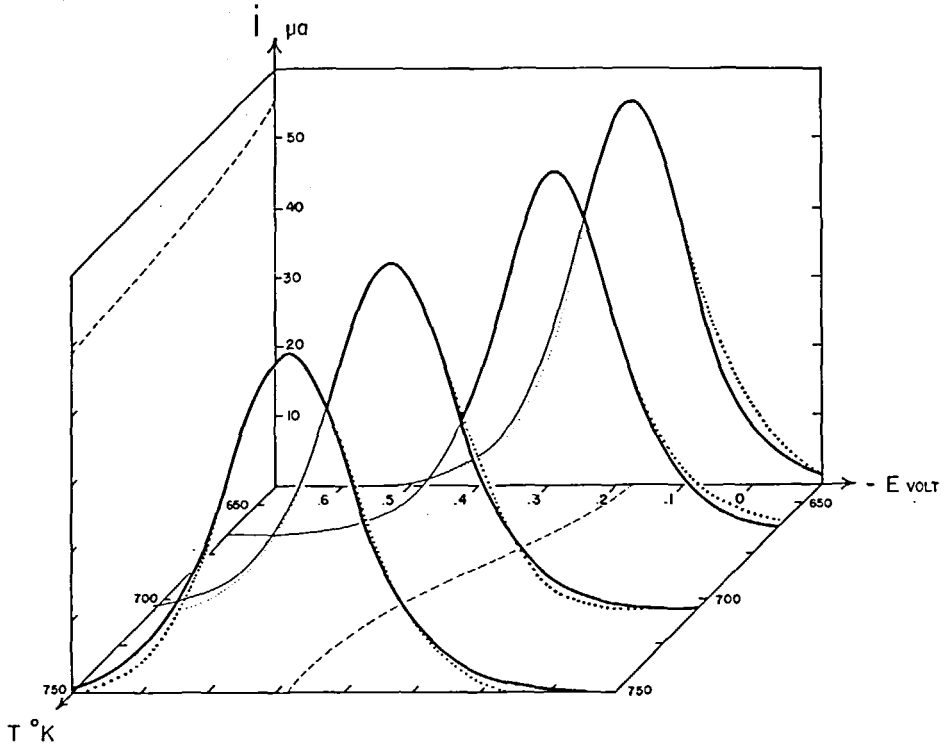

FIGURE 30. Thin-layer current-potential curves for Cr(III) in LiCl-KCl eutectic melt.[33] Dotted curves: experimental points; Solid curves: graphs of Equation 2. Experimental conditions: the reactant solution contained $CrCl_3$, LiCl, and 51% KCl, as follows:

T, °K	$10^3 \times C_{CrCl_3}$, F	$10^3 \times V$, cm³
640	5.71	5.35
669	5.66	5.40
719	5.57	5.28
754	5.51	4.96

A = 1.00 cm²; |r| = 4 mV sec⁻¹; the reference electrode was Ag/0.07 *F* AgCl in the LiCl-KCl melt.

The relationships among these species are depicted in Equation 166:

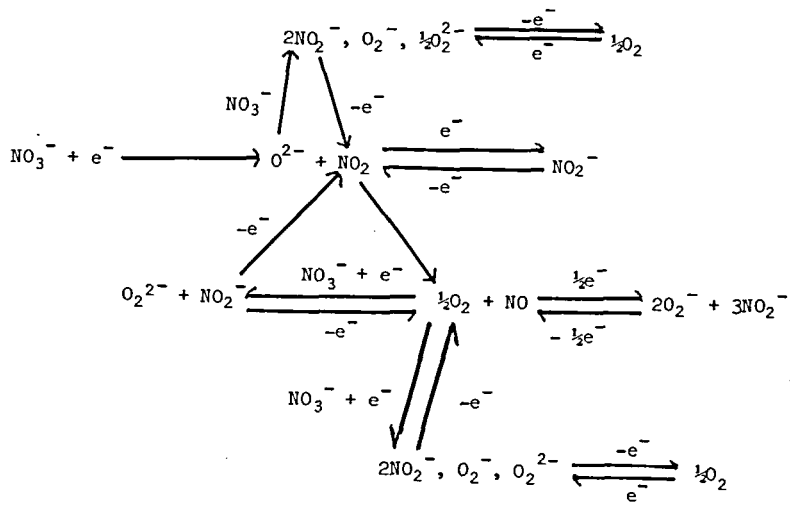

(166)

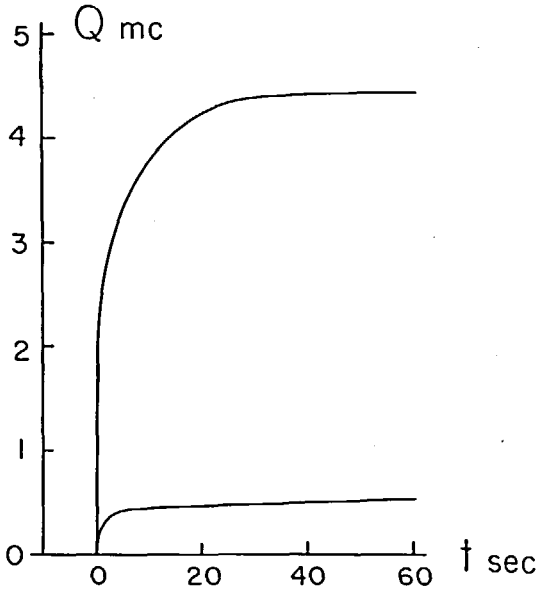

FIGURE 31. Thin-layer coulometric charge-time curve for Cr(III) in LiCl-KCl eutectic melt.[33] Experimental conditions: the upper curve was obtained with a solution containing 7.6 x 10^{-3} *F* $CrCl_3$, 51% KCl, and LiCl; A = 1.00 cm^2; ℓ = 5.2 x 10^{-3} cm; T = 723°K; the initial and final potentials were −0.300 and −0.900 V vs. a Pt/(0.1 *F*) $PtCl_4^{2-}$ reference electrode in the LiCl-KCl eutectic melt. The lower curve is a blank.

Studies of electrode kinetics in melts by means of thin-layer electrode appear to offer the same advantages of simplicity, accuracy, and surface reproducibility as in aqueous solutions (Part IV, Section B-1). Variations in double-layer structure resulting from changes in melt composition and temperature have a profound effect on the rates and stoichiometries of irreversible electrode reactions, suggesting a fascinating area for future experimental and theoretical study. For instance, the reduction of IO_3^- in $NaNo_3$-KNO3 and LiCl-KCl eutectic melts containing various Lux-Flood acids is influenced by adsorption of the products, as was the case for aqueous solutions,[75] although the detailed stoichiometric acid-base and interfacial behavior differ.

Acknowledgments

Acknowledgment is made to the donors of the Petroleum Research Fund, administered by the American Chemical Society, and to the National Science Foundation for support of many of the studies described in this review.

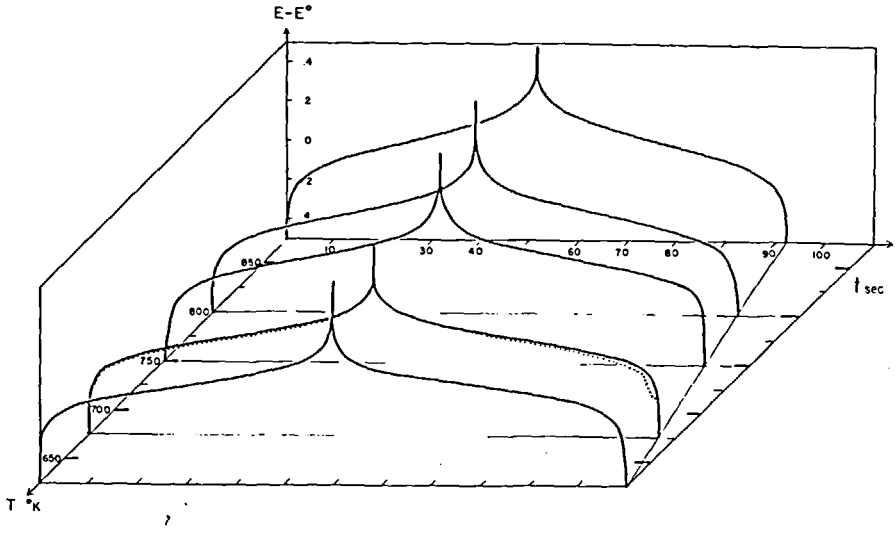

FIGURE 32. Thin-layer chronopotentiograms for the Cr(III)-Cr(II) couple in LiCl-KCl eutectic melt.[33] Experimental conditions: the solution contained 5.71 x 10^{-3} *F* $CrCl_3$, 51% KCl, and LiCl; A = 1.00 cm^2; i = 5.00 x 10^{-5} A; T = 641°K; V = 5.39 x 10^{-3} cm^3; and the reference electrode was Ag/0.07 *F* AgCl in the LiCl-KCl eutectic melt.

REFERENCES

1. Hubbard, A. T. and Anson, F. C., The theory and practice of electrochemistry with thin layer cells, in *Electroanalytical Chemistry*, Vol. 4, Bard, A. J., Ed., Marcel Dekker, New York, 1971, 129.
2. Hubbard, A. T., *J. Electroanal. Chem.*, 22, 165 (1969).
3. Hubbard, A. T., Ph.D. thesis, California Institute of Technology, Pasadena, Calif., 1967.
4. Carslaw, H. S. and Jaeger, J. C., *Conduction of Heat in Solids*, 2nd ed., Clarendon Press, Oxford, 1959.
5. Hubbard, A. T. and Anson, F. C., *Anal. Chem.*, 38, 58 (1966).
6. Lai, C. N. and Hubbard, A. T., *Inorg. Chem.*, 11, 2081 (1972).
7. Delahay, P., *Double Layer and Electrode Kinetics*, Interscience, New York, 1965.
8. Lau, A. L. Y. and Hubbard, A. T., *J. Electroanal. Chem.*, 33, 77 (1971).
9. Lane, R. F. and Hubbard, A. T., *J. Phys. Chem.*, in press.
10. Lane, R. F. and Hubbard, A. T., *J. Phys. Chem.*, in press.
11. Hubbard, A. T. and Anson, F. C., *Anal. Chem.*, 38, 1601 (1966).
12. Tom, G. M. and Hubbard, A. T., *Anal. Chem.*, 43, 671 (1971).
13. Christensen, C. R. and Anson, F. C., *Anal. Chem.*, 35, 205 (1963).
14. Delahay, P., *New Instrumental Methods in Electrochemistry*, Interscience, New York, 1954.
15. Anderson, L. B. and Reilley, C. N., *J. Electroanal. Chem.*, 10, 295 (1965).
16. Anderson, L. B., McDuffie, B., and Reilley, C. N., *J. Electroanal. Chem.*, 12, 477 (1966).
17. Reilley, C. N., *Pure Appl. Chem.*, 18, 137 (1968).
18. Hubbard, A. T. and Anson, F. C., *Anal. Chem.*, 36, 723 (1964).
19. Oglesby, D. M., Omang, S. H., and Reilley, C. N., *Anal. Chem.*, 37, 1312 (1965).
20. Schmidt, E. and Gygax, H. R., *Helv. Chim. Acta*, 48, 1180 (1965).
21. McClure, J. C. and Maricle, D. L., *Anal. Chem.*, 39, 236 (1967).
22. Cushing, J. R. and Hubbard, A. T., *J. Electoanal. Chem.*, 23, 183 (1969).
23. Schmidt, E. and Gygax, H. R., *Chimia*, 16, 165 (1962).
24. Sheaffer, J. C. and Peters, D. G., *Anal. Chem.*, 42, 430 (1970).
25. Murray, R. W., Heineman, W. R., and O'Dom, G. W., *Anal. Chem.*, 39, 1666 (1967).
26. Heineman, W. R., Burnett, J. N., and Murray, R. W., *Anal. Chem.*, 40, 1970 (1968).
27. Yildiz, A., Kissinger, P. T., and Reilley, C. N., *Anal. Chem.*, 40, 1018 (1968).
28. Schwabe, K. and Schwenke, W., *Electrochim. Acta*, 9, 1003 (1964).

29. Blaedel, W. J., Olson, C. L., and Sharma, L. R., *Anal. Chem.*, 35, 2100 (1963).
30. Klatt, L. N. and Blaedel, W. J., *Anal. Chem.*, 38, 879 (1966); 39, 1065 (1967).
31. Blaedel, W. J. and Boyer, S. L., *Anal. Chem.*, 43, 1538 (1971).
32. Hubbard, A. T. and Anson, F. C., *Anal. Chem.*, 40, 615 (1968).
33. Zajicek, L. P. and Hubbard, A. T., University of Hawaii, unpublished results.
34. Hubbard, A. T., Osteryoung, R. A., and Anson, F. C., *Anal. Chem.*, 38, 692 (1966).
35. Goldberg, I. B., Bard, A. J., and Feldberg, S. W., *J. Phys. Chem.*, 76, 2550 (1972).
36. Goldberg, I. B., Bard, A. J., and Feldberg, S. W., *J. Phys. Chem.*, 75, 3281 (1971).
37. Schoeffel, J. A. and Hubbard, A. T., University of Hawaii, unpublished results.
38. Somorjai, G. A. and Farrell, H. H., in *Advances in Chemical Physics*, Vol. 20, Prigogine, I. and Rice, S. A., Eds., Interscience, New York, 1971, 215.
39. Chang, C. C., *Surface Sci.*, 25, 53 (1971).
40. Siegbahn, K. *et al., ESCA; Atomic, Molecular and Solid State Structure Studied by Means of Electron Spectroscopy*, Almqvist and Wiksells, Uppsala, 1967.
41. Madey, T. E. and Yates, J. T., Jr., *J. Vac. Sci. Technol.*, 8, 525 (1971).
42. Ishikawa, R. M. and Hubbard, A. T., University of Hawaii, unpublished results.
43. Brophy, J. J., *Basic Electronics for Scientists*, 2nd ed., McGraw-Hill, New York, 1972, 303.
44. Malmstadt, H. V., Enke, C. G., and Toren, E. C., *Electronics for Scientists*, W. A. Benjamin, New York, 1962, 341.
45. Hubbard, A. T. and Anson, F. C., *Anal. Chem.*, 38, 1887 (1966).
46. Peychal-Heiling, G. and Wilson, G. S., *Anal. Chem.*, 43, 545 (1971); 43, 550 (1971).
47. Lau, A. L. Y. and Hubbard, A. T., *J. Electroanal. Chem.*, 24, 237 (1970).
48. Christensen, C. R. and Anson, F. C., *Anal. Chem.*, 36, 495 (1964).
49. Oglesby, D. M., Johnson, J. D., and Reilley, C. N., *Anal. Chem.*, 38, 385 (1966).
50. McDuffie, B. and Reilley, C. N., *Anal. Chem.*, 38, 1881 (1966).
51. McDuffie, B., Anderson, L. B., and Reilley, C. N., *Anal. Chem.*, 38, 883 (1966).
52. Laviron, E., *J. Electroanal. Chem.*, 39, 1 (1972).
53. Konopka, S. J. and McDuffie, B., *Anal. Chem.*, 42, 1741 (1970).
54. Schmidt-Weimar, H. G., *Ber. Bunsenges. Phys. Chem.*, 7, 97 (1967).
55. Hubbard, A. T. and Anson, F. C., *J. Electroanal. Chem.*, 9, 163 (1965).
56. Osteryoung, R. A. and Anson, F. C., *Anal. Chem.*, 36, 975 (1964).
57. Schmidt, E. and Gygax, H. R., *Helv. Chim. Acta*, 48, 1178 (1965).
58. Schmidt, E. and Wüthrich, N., *Helv. Chim. Acta*, 50, 2058 (1967).
59. Schmidt, E. and Gygax, H. R., *Helv. Chim. Acta*, 48, 1584 (1965).
60. Schmidt, E. and Gygax, H. R., *Helv. Chim. Acta*, 49, 733 (1966).
61. Schmidt, E. and Gygax, H. R., *Helv. Chim. Acta*, 49, 1105 (1966).
62. Schmidt, E. and Gygax, H. R., *J. Electroanal. Chem.*, 12, 300 (1966).
63. Zajicek, L. P. and Hubbard, A. T., *J. Electrochem. Soc.*, 116, 90C (1969).
64. Lingane, J. J., *J. Electroanal. Chem.*, 7, 94 (1964).
65. Kern, D. M. H. and Orlemann, E. F., *J. Am. Chem. Soc.*, 71, 2102 (1949).
66. Feldberg, S. W. and Auerbach, C., *Anal. Chem.*, 36, 505 (1964).
67. Schuldiner, S., Warner, T. B., Anson, F. C., and Osteryoung, R. A., *Anal. Chem.*, 36, 2510 (1964).
68. Balashova, N. A. and Kazarinov, V. E., *Russ. Chem. Rev.*, 34, 730 (1965).
69. Newson, J. N. and Riddiford, A. C., *J. Electrochem. Soc.*, 108, 699 (1961).
70. Osteryoung, R. A., *Anal. Chem.*, 35, 1100 (1963).
71. Osteryoung, R. A., Lauer, G., and Anson, F. C., *J. Electrochem. Soc.*, 110, 926 (1963).
72. Schuldiner, S. and Presby, C. H., *J. Electrochem. Soc.*, 111, 457 (1964).
73. Zambonin, P. G. and Jordan, J., *Anal. Lett.*, 1, 1 (1968).
74. Zambonin, P. G., *Anal. Chem.*, 43, 1571 (1971).
75. King, D. M. and Anson, F. C., *Anal. Chem.*, 34, 362 (1962).